

**PREFERRED REVERSAL PATHS CAUSED BY A HETEROGENEOUS  
CONDUCTING LAYER AT THE BASE OF THE MANTLE**

By

Simona E.O. Costin

B.A.Sc.(Geological and Geophysical Engineering), University of Bucharest, Romania

A THESIS SUBMITTED IN PARTIAL FULFILLMENT OF  
THE REQUIREMENTS FOR THE DEGREE OF  
MASTER OF SCIENCE

in

THE FACULTY OF GRADUATE STUDIES  
DEPARTMENT OF EARTH AND OCEAN SCIENCES (GEOPHYSICS)

We accept this thesis as conforming  
to the required standard

THE UNIVERSITY OF BRITISH COLUMBIA

August 2003

© Simona E.O. Costin, 2003

In presenting this thesis in partial fulfillment of the requirements for an advanced degree at the University of British Columbia, I agree that the Library shall make it freely available for reference and study. I further agree that permission for extensive copying of this thesis for scholarly purposes may be granted by the head of my department or by his or her representatives. It is understood that copying or publication of this thesis for financial gain shall not be allowed without my written permission.

Department of Earth and Ocean Sciences (Geophysics)  
The University of British Columbia  
129-2219 Main Mall  
Vancouver, Canada  
V6T 1Z4

Date:

Oct. 12, 2003

## **Abstract**

Paleomagnetic data from sedimentary and volcanic rocks suggest that the positions of the Virtual Geomagnetic Pole (VGP) during polarity reversals over the past few million years are confined to longitudes through the Americas and Asia. In this study I examine the possibility that lateral conductivity variations in the lowermost region of the mantle contribute to the geographical distribution of the reversal paths. The conductivity model consists of a thin layer of material with variable electrical properties which accumulates in the core-mantle boundary region. The pattern of conductivity relies on the geodynamic predictions of the boundary topography and is in good agreement with the seismological observations of heterogeneities at the core-mantle boundary. Temporal variations in the dipole field during a reversal generate electric currents in the conductive layer, which in turn produce a secondary magnetic field. Superposition of the secondary field on a transition field affects the declination and inclination of the magnetic field at the surface and thereby changes the position of the VGP during a reversal. My results predict preferred reversal paths over North America for uniform sampling of testing sites. This corresponds to one preferred path previously observed in the geological records. In addition, preferred paths over the Americas and Asia are predicted when using the same testing sites as the paleomagnetic database, compatible with the distribution of paths given by the observations.

## Table of Contents

<b>Abstract</b>	<b>ii</b>
<b>List of Tables</b>	<b>v</b>
<b>List of Figures</b>	<b>vi</b>
<b>Acknowledgements</b>	<b>ix</b>
<b>1 INTRODUCTION</b>	<b>1</b>
<b>2 THEORETICAL BACKGROUND</b>	<b>11</b>
2.1 Definition and Calculation of VGP . . . . .	11
2.2 Electromagnetic Background: Maxwell's Equations . . . . .	13
2.3 Potential Fields, Spherical Harmonics and Legendre Functions . . . . .	14
2.4 Orthogonality of Spherical Harmonics, Schmidt Normalization and Gauss Coefficients . . . . .	16
2.5 Vector Spherical Harmonics . . . . .	17
<b>3 THE PROBLEM</b>	<b>20</b>
3.1 A Conceptual Model . . . . .	20
3.2 Formulation of the Problem . . . . .	25
3.3 Boundary Conditions . . . . .	26
3.4 Calculation of the Electric Current in the Layer . . . . .	27
3.5 Solution for the Magnetic Perturbation Using a Thin Sheet Approximation	32

<b>4</b>	<b>CONDUCTIVITY MODELS AND RESULTS</b>	<b>37</b>
4.1	VGP Paths Based on CMB Topography . . . . .	37
4.2	Observational Constraints on the Conductivity Model . . . . .	40
4.3	VGP Paths Obtained with a Constrained Model . . . . .	51
<b>5</b>	<b>ADDITIONAL RESULTS</b>	<b>54</b>
5.1	Tests on the Paleomagnetic Database . . . . .	54
5.2	Brief Description of the Transition Field Model . . . . .	58
5.3	VGP Paths Obtained When a Background Non-Dipole Field Is Included	61
<b>6</b>	<b>DISCUSSION AND CONCLUSIONS</b>	<b>67</b>
	<b>References</b>	<b>72</b>

## **List of Tables**

Table 4.1 Coefficients for the conductivity models .....	52
Table 4.1 Gauss coefficients of the perturbation field .....	52

## List of Figures

1.1. Reversal paths as suggested by observations .....	4
1.2 Possible structures at CMB .....	7
2.1 The main elements of the magnetic field .....	12
3.1 Schematic illustration of the conductive layer .....	21
3.2 The conductivity model (TC) based on the geodynamic topography of the boundary .....	23
3.3 Complex structures at CMB .....	35
4.1 Geographical distribution of the sites used to test the VGP paths .....	37
4.2 VGP paths obtained using the TC model .....	38
4.3 Secular variation observations .....	40
4.4 Observations and model predictions for the $g_2^3$ Gauss coefficients .....	41
4.5 Observations and model predictions for the $h_2^3$ Gauss coefficients .....	42
4.6 Observations and model predictions for the equatorial dipole .....	44
4.7 Historical field model .....	45
4.8 Comparison between the historical field and model predictions for the $Y_3^2$ spherical harmonic coefficients .....	46
4.9 Comparison between the historical field and model predictions for the $Y_1^1$ spherical harmonic coefficients .....	47
4.10 The conductivity model (CC) obtained using new constraints .....	49
4.11 VGP paths obtained using the CC model .....	50
5.1 VGP paths obtained for volcanic database .....	54

5.2 VGP paths obtained for ODP database .....	55
5.3 VGP paths obtained from a compiled database .....	56
5.4 Geomagnetic spectrum for the non-dipole field .....	60
5.5 VGP paths obtained with a random background field .....	61
5.6 VGP paths obtained with a random background field .....	62
5.7 VGP paths obtained for different reversal periods .....	64



*"Keep true to the dreams of thy youth"*

*Friederich von Schiller*

## Acknowledgements

Here are the acknowledgement nominees:

- Category: Best Director:

*Bruce Allen Buffett, Allen Buffett Bruce, Buffett Bruce Allen*

For being the wisest, nicest, most helpful, incredible supervisor.

- Category: Best Supportive Professors:

*Michael Bostock, Doug Oldenburg, Stuart Sutherland, Tad Ulrych*

For helping and trusting me, for your natural kindness and sense of humor, for all the interesting things I have learned from you. Special people like you make the EOS department wonderful.

- Category: Best Supportive Peers:

*Charly Georg Bank, Christophe Hyde, Daniel Trad, Olga Zatsepina*

For *Friendship* has many names.

- Category: Best Office Mates:

*Matt Keith Davie, Nicolas Lhomme, Joanna Kim Welford*

For all the inspired conversations we had, for your pleasant companionship in the office and *ailleurs*.

- Category: Best Support Across-the-Miles:

*Barry Curtis Zelt*

For the *mystic* and *real* you.

- Category: The-Last-But-Not-the-Least:

*Jon Edwin Mound*

For being such a nice *bridge* partner, for Samwise of the Shire, the *solitude* and the .tex files.

- Category: Most Special Thanks

*T.A. & T.M., and D.P., and O. & V. Costin*

For the hot dinners you've been waiting me with. For your unabridged understanding, loving, support and help.

## Chapter 1

### INTRODUCTION

Planetary magnetic fields are widely believed to be generated and maintained by convective flows in the internal regions of the planets, resulting in the well known dynamo action. In the case of the Earth, the dynamo effect is believed to be generated in the fluid outer core, where churning and twisting flows of highly conductive material continually regenerate the magnetic field. In the absence of regeneration the magnetic field would decay in about 20,000 years. The convection in the outer core is driven by thermal and compositional buoyancy sources as the core slowly cools and solidifies. These buoyancy forces drive fluid motions, which are acted on by the Coriolis force to produce helical flows. It is thought that these helical motions re-generate the magnetic field. Fluid flows in the core are highly non-linear and chaotic, causing a complex temporal variability of the geomagnetic field [*Glatzmaier and Roberts, 1995*].

Although the time variation of the magnetic field is precisely observed in our days, we have limited insight into this variation from direct observations due to the slow rate of change in the field. Most of our knowledge about the behavior of the magnetic field on a geological time scale comes from the paleomagnetic records.

When a rock containing magnetic minerals cools through the Curie temperature, it retains the characteristics of the ambient magnetic field. This primary magnetization provides information about the direction and intensity of the field at the time of rock formation. The rock may subsequently acquire a secondary magnetization, however, the characteristics of the primary magnetization are important to paleo-magnetists. The

primary magnetization is usually thermo-remanent magnetization in igneous rocks and depositional, post-depositional, or occasionally chemical remanent magnetization, in sedimentary rocks [Merrill and McElhinny, 1983]. Generally speaking, records from volcanic rocks are easier to interpret, since the radioactive dating of the sample provides a reliable age. Lava records usually give information about one particular geomagnetic event. In contrast, observations from sediments provide a continuous record, which sometimes captures several paleomagnetic events, but determination of the magnetization time is more difficult and occasionally unreliable [Merrill and McElhinny, 1983].

One of the most puzzling features of the magnetic field was determined by looking at the magnetization in rocks and archeological clay objects. Measurements of the magnetization revealed that the Earth's magnetic field varies in strength and direction, occasionally changing its polarity. Reversals of the magnetic field polarity were observed for the first time at the beginning of the last century. The initial observations were made by David and later Brunhes in rocks baked by lava flows. These authors were the first to report the discovery of remanent magnetization that was opposite to the orientation of the present field. Over the following decades, subsequent studies on volcanic rocks have revealed that the Earth's magnetic field has reversed itself in the past, *e.g.* Mercatón [1926], Matuyama [1929], Roche [1951] (see Merrill and McElhinny, 1983 for a complete review). Systematic studies have defined a polarity time-scale through joint measurements of magnetic polarity and radioactive age on lava flows. The first time scale, put together by Cox *et al.* [1964], showed magnetic polarity reversals with a rough periodicity of about one million years. Opdyke *et al.* [1966] later found evidence for magnetic reversals in deep-sea sediment cores, with timing and magnetic reversals pattern similar to the one inferred from volcanic rocks on land. However, as new data was made available, it became apparent that there was no simple periodicity of the magnetic reversals.

Records have revealed that the time intervals for the same magnetic polarity are sometimes long, up to one million years, or quite short, to less than a hundred thousand years [Merrill and McElhinny, 1983]. Within a long period of predominant polarity there are much shorter intervals of reversed polarity. According to their length, the intervals have been named chrons, subchrons or superchrons. The paleomagnetic record has also shown events known as excursions during which the reversal was either aborted or of extremely short duration. The currently accepted geomagnetic polarity time-scale was produced by Cande and Kent [1995] based on magnetic anomalies determined in sea-floor sediments.

During a polarity reversal, the direction of the geomagnetic field changes in time by about  $180^\circ$ . The Virtual Geomagnetic Pole (VGP), conventionally defined as the pole of a dipolar field which gives the same observables at a site as the natural field, follows a particular geographic path from one hemisphere to another.

In the last decades, several compilations have drawn attention to a more subtle morphology of the transition fields [e.g. Laj *et al.*, 1991, 1992; Clement, 1991; Hoffman, 1992]. These works have revealed that the VGP paths during a reversal are not random, but are confined to two particular zones of longitude, covering Asian and American regions. Initially, the compilations showing preferred VGP paths came from measurements on deep-sea cores (Figure 1.1). The existence of preferred paths was disputed by a number of authors who questioned the reliability of the sedimentary records [e.g., Langereis *et al.*, 1992] and the adequacy of the geographic distribution of sites [Valet *et al.*, 1992]. The suggestion of preferred paths was subsequently challenged by Prévot and Camps [1993], using data from volcanic rocks. However, more recent compilations made by Love on lava data have found that volcanic records give transitional VGPs which tend to fall along American and Asian longitudes [Love, 1998; Gubbins and Love, 1998; Love, 2000], roughly consistent with the sedimentary data.

The veracity of the confined VGP paths has not been resolved yet. But if the preferred

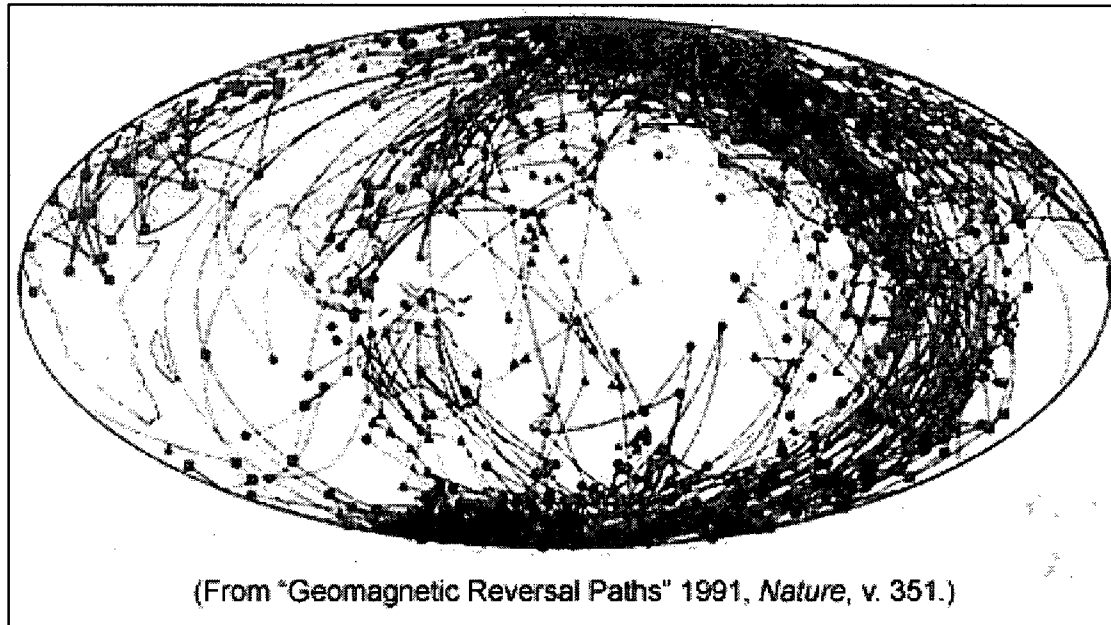


Figure 1.1: Reversal paths as suggested by *Laj et al.* [1991].

paths really exist, then their persistence over millions of years suggests that structures in the mantle, with large characteristic time scales control this phenomenon [e.g., *Gubbins*, 1994]. Since the idea of confined reversal paths was first reported, numerous explanations have been proposed. *Laj et al.* [1991] noted a correlation between the VGP paths and P-wave anomalies in the lower mantle, while *Constable* [1992] observed that one of the preferred paths could be explained by decreasing the axial dipole of the present-day field; a change in sign in the non-axial-dipole terms yields the other preferred path. The flux patches in the present-day field that contribute to the preferred paths in the study of *Constable* appear to be persistent in the paleomagnetic field [*Gubbins and Kelly*, 1993; *Johnson and Constable*, 1998]. This could account for the consistency of the reversal paths in the past. *Gubbins and Coe* [1993] also attributed longitude-confined VGP paths

to flux patches that migrate during a reversal. They concluded that the American and Asian paths are equally probable.

Other studies appeal directly to core-mantle coupling to explain the tendency of the VGP paths to follow the same meridians. *Gubbins and Sarson* [1994] showed that heterogeneous heat flow at the core-mantle boundary (CMB) can influence the pattern of flow in the core, which would affect the transitional field morphology and possibly yield preferred VGP paths along the longitudes where downwellings occur. An alternate model, proposed by *Runcorn* [1992], attributes the geometrical confinement of the reversal paths to the presence of a conducting shell in the  $D''$  region of the mantle, beneath the Pacific Ocean. Runcorn argued that the existence of the conducting layer would explain the observed low level of secular variation in the Pacific by electromagnetic screening. Moreover, the electrical currents induced in the shell by a reversing dipole can generate an electromagnetic torque that rotates the core until the reversing dipole path coincides with one of the meridians that border the conducting shell [*Runcorn*, 1992; *Herrero-Bervera and Runcorn*, 1997]. *Aurnou et al.* [1996] quantitatively assessed Runcorn's idea using a distribution of electrical conductivity based on shear-wave tomography. They found that preferred reversal paths could be obtained through this mechanism, although this result was later challenged by *Brito et al.* [1999], who concluded that the electromagnetic torque due to the heterogeneity of  $D''$  is too small to rotate the core and thus no preferred paths would emerge. *Holme* [2000] also argued against Runcorn's mechanism for VGP paths, on the grounds that the required conductance is unrealistically high.

All of the aforementioned studies were motivated by observations of complex, heterogeneous structures in the lowermost part of the mantle (see Figure 1.2). Seismological observations show increased levels of heterogeneity in the lowermost 200 km, indicating lateral variations in the physical properties in this region [*Lay et al.*, 1998]. Much narrower regions of heterogeneity have been detected within a few tens of kilometers of the



CMB in large areas [Garnero and Helmberger, 1995, 1996]. These regions are known as ultra-low velocity zones (ULVZ), because they are characterized by decreases in P and S velocities up to 30%. Roughly one-third of the investigated areas display wave velocity depressions [Garnero and Jeanloz, 2000]. A map of regions investigated for ULVZs is displayed in Figure 3.3 [Garnero *et al.*, 1998]. Regions in red denote ULVZ detections, whereas regions in blue indicate no evidence for ULVZ structures. The thickness of these anomalous structures is variable (5 - 40 km) and has been determined using waveform modelling [Garnero and Helmberger, 1996]. The origin of ULVZ structures may be the partial melt of mantle material [Williams and Garnero, 1996], due to thermal anomalies such as enhanced heat flux from the core [Williams *et al.*, 1998], or viscous heating [Steinbach and Yuen, 1999]. In addition to partial melt, changes in bulk composition may also decrease the seismic velocities [Garnero, 2000]. Possible explanations for deviations in bulk composition include chemical reactions between the silicate mantle and the liquid core alloy [Knittle and Jeanloz, 1989, 1991], iron enrichment of partial melt under lower mantle conditions [Knittle, 1998], or grain boundary wetting of the silicate minerals by the iron alloy originating in the outer core [Poirer and Le Mouél, 1992; Poirer *et al.*, 1998]. These mechanisms predict a complex chemical constitution of the lower mantle, and imply that the lowermost part of the mantle is composed of conducting material. However, the predicted values of electrical conductivity in  $D''$  and thickness of the conducting region vary from one work to another.

Buffett *et al.* [2000] attempt to explain the complex structure at the CMB by suggesting the presence of silicate sediments accumulating at the top of the core as the result of secular cooling and solidification of the core. The chemical equilibrium of the liquid core is disturbed by the segregation of lighter elements as the (solid) inner core grows. This equilibrium could be re-established by the expulsion of silicates from the liquid core. The buoyancy of silicates in liquid iron suggests that sediments accumulate in the

topographic highs, where the boundary is displaced radially towards the mantle. These regions act as basins from the standpoint of the core material and are predicted to exhibit high conductivities, owing to the presence of interstitial liquid iron in the sediment layer. The iron content of the layer can be as large as 50%, which yields conductivities of the order of  $10^5$  S/m. Alternatively, the model predicts that regions where the boundary is pushed towards the core are not favourable for sediment accumulation. These regions would have electrical conductivities more like typical mantle materials [Shankland *et al.*, 1993], which are orders of magnitude lower than the values in the sediment layer. Accordingly, the sediment model predicts the existence of a layer with variable conductivity and relates the position of the conducting regions to the CMB topography. The presence of a region of enhanced conductivity near the core-mantle boundary is compatible with observations of the Earth's nutation [Buffett, 1992] and could account for the velocity drop in the ULVZs.

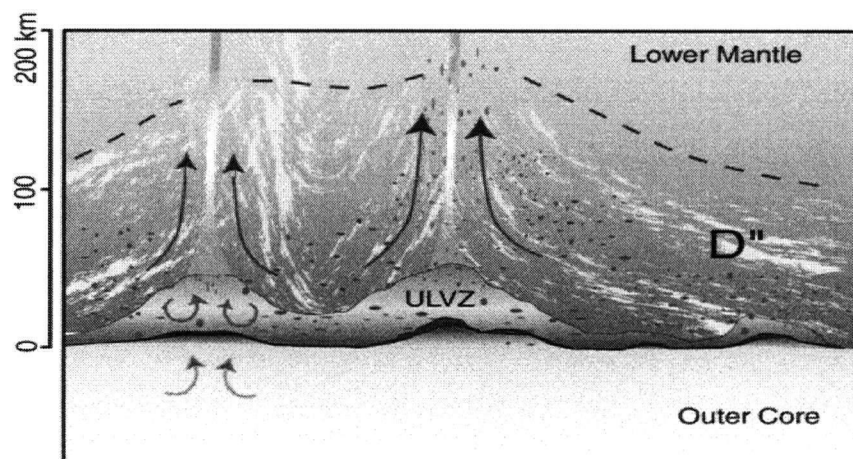


Figure 1.2: Possible complex structures at the CMB [Garnero, 2000]. The ULVZ is associated with partial melt and chemical heterogeneity. The sharpness of the CMB is constrained to be less than 4 km.

In this work, I assume the presence of a laterally varying conducting layer at the

base of the mantle. During a magnetic polarity reversal, the dipole component of the Earth's magnetic field decreases in time and therefore electrical currents are generated in the conductive parts of the layer. Circulation of these currents in the basal layer induces a secondary magnetic field. Superposition of the secondary field on the magnetic field generated by the geodynamo changes the characteristics of the field and might yield preferred reversal paths due to the new configuration of the transition field. The goal of this thesis is to assess the effects of the secondary field on the VGP paths.

The next chapter of the thesis presents the theoretical framework for this problem and provides the basic formulae, including the definition and calculation of the VGP. The third chapter formulates the problem from a conceptual point of view and develops quantitative solutions. It explains the geometry and parameters of the model and the physics of this problem. The interaction between the electric and magnetic fields are described by Maxwell's equations. Simplifications of these equations are achieved by assuming a low frequency approximation. The fields are represented in terms of poloidal and toroidal potentials. The scalar and vector functions in this study are described employing the spherical harmonic expansion with Schmidt quasi-normalized coefficients. The solution to the magnetic induction problem is found using a thin sheet approximation. Computations show that the secondary field depends on the physical and geometrical parameters of the layer and on the variation of the dipole field. The field generated by the layer is characterized by a finite sum of spherical harmonic components. The most important terms are upward continued to define the magnetic field at the surface during a polarity reversal.

The fourth chapter uses the calculated magnetic field to determine synthetic paleomagnetic data, *i.e.*, the magnetic inclination and declination, at a set of random locations around the globe. The synthetic data yields the VGP at each site. The resultant VGP paths are binned in histograms of  $20^\circ$  longitude. To gain a better understanding of how

the perturbation affects the VGP paths, I consider the effect of each term of the perturbation field separately. The results show that the distribution of the VGP reversal paths is different for each component of the perturbation field. When the entire perturbation is considered, the histograms of computed VGP longitudes reveal preferred paths covering American and Greenland longitudes. To improve the fit to the data, the initial model is refined based on modern observations. I consider the secular variation of the internal field and compare it with the model predictions of the magnetic field induced in the layer. I assume that the observed secular variation signal includes the signature of the perturbation generated in the conductive layer at the base of the mantle. The model parameters are adjusted such that the predicted coefficients reproduce the same variability as the observations. The constraints deduced from fitting the observations are adopted in a new conductivity model which is now constrained not only by the geodynamic topography parameters but also by the secular variation data. Subsequently, a new dataset of paleomagnetic observations is generated for the same random locations. The distribution of VGP reversal paths obtained with the new conductivity model reveals preferred paths covering North American longitudes, in partial agreement with the observations, which usually find two preferred paths. However, non-uniform sampling, which mimics the distribution of sites in the paleomagnetic database, leads to two reversal paths, in agreement with the observations.

In the last chapter the transition field is modelled by considering other non-dipolar terms besides the perturbation field. I use the secular variation statistical model of *Constable and Parker* [1988] to describe the non-dipolar terms. These terms define a 'background' field from the standpoint of the magnetic perturbation. I am interested in determining whether the perturbation field rises above the natural variability of the Earth's magnetic field during a reversal. The transition field is devised such that each different realisation of the statistical model represents a different reversal of the magnetic

field. Statistics show that during a reversal, when the dipole field weakens or disappears completely, the amplitude of the perturbation field is big enough to leave its signature on the VGP paths. The distribution of the VGP paths in this case reveals again the preferred paths through North America, confirming the results in the previous chapter. In addition, the results in the fifth chapter show that the duration of the reversal and the number of reversals are other factors which influence the distribution of the VGP reversal paths.

## Chapter 2

### THEORETICAL BACKGROUND

#### 2.1 Definition and Calculation of VGP

The Virtual Geomagnetic Pole corresponds to the pole of a geocentric dipolar field which gives the direction of magnetization at an observation site [Jacobs, 1984]. Therefore, the calculation of VGP assumes a dipolar field, which is not strictly true. On the other hand, the VGP can be defined from the direction of magnetization at a single site. The geographic co-ordinates of the VGP (latitude,  $\lambda^1$ , longitude,  $\phi^1$ ) are calculated using the co-ordinates of the observation site (latitude,  $\lambda$ , longitude,  $\phi$ ) and the paleomagnetic direction measured at the site (declination,  $D_m$ , inclination,  $I_m$ ). From the spherical geometry, the following relationships are obtained [Merrill and McElhinny, 1983]

$$\begin{aligned}\sin \lambda^1 &= \sin \lambda \cos \theta + \cos \lambda \sin \theta \cos D_m, & \text{for } (-90^\circ \leq \lambda^1 \leq +90^\circ) \\ \phi^1 &= \phi + \beta, & \text{when } \cos \theta \geq \sin \lambda \sin \lambda^1 \\ \phi^1 &= \phi + 180 - \beta, & \text{when } \cos \theta \leq \sin \lambda \sin \lambda^1 \\ \sin \beta &= \sin \theta \sin D_m / \cos \lambda^1, & \text{for } (-90^\circ \leq \beta \leq +90^\circ).\end{aligned}\tag{2.1}$$

The paleo-colatitude  $\theta$  of the site is defined relative to the position of the VGP and is determined by the paleomagnetic inclination  $I_m$ . The  $\hat{r}$  and  $\hat{\theta}$  components of a magnetic dipolar field  $\mathbf{B}$  are defined in terms of the paleo-colatitude  $\theta$  by

$$B_r = -\frac{2\mu_0 p \cos \theta_m}{4\pi R^3}\tag{2.2}$$

and

$$B_\theta = -\frac{\mu_0 p \sin \theta_m}{4\pi R^3}, \quad (2.3)$$

where  $p$  is the dipole moment,  $\mu_0 = 4 \times \pi 10^{-7}$  H/m is the permeability of free space,  $R$  is the distance to the source and  $\theta_m$  is the magnetic co-latitude. Paleo-magnetists often assume that  $\theta_m$  is a reasonable estimate of the co-latitude  $\theta$  because statistics show that inclinations from the Earth's magnetic field (which is predominantly dipolar) cluster around the values expected for a geocentric axial dipolar field [Tauxe, 2002]. From Figure 2.1, it follows that  $\tan I_m = B_r/B_\theta$ , and a straightforward substitution leads to  $\tan I_m = 2 \cot \theta_m$ .

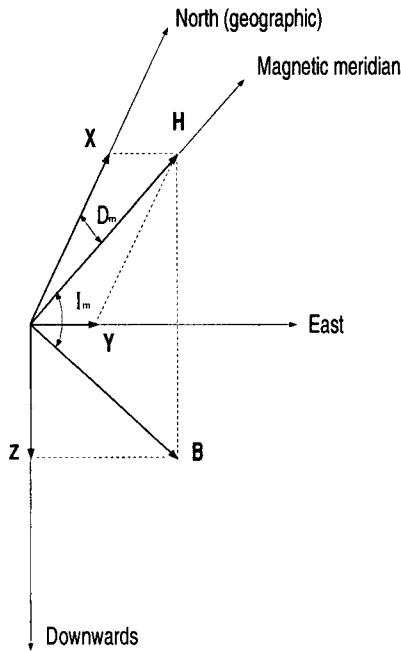


Figure 2.1: The main elements of the magnetic field  $\mathbf{B}$ . The horizontal component  $\mathbf{H}$  of the magnetic field can be resolved into two components,  $\mathbf{X} = -\mathbf{B}_\theta$ , northwards,  $\mathbf{Y} = \mathbf{B}_\phi$ , eastwards. The vertical component of  $\mathbf{B}$  is  $\mathbf{Z} = -\mathbf{B}_r$ . The deviation of a compass needle from the true north is the *declination*  $D_m$ . The angle  $I_m$  between the magnetic field  $\mathbf{B}$  and the horizontal component  $\mathbf{H}$  is called *inclination* or *dip*.

## 2.2 Electromagnetic Background: Maxwell's Equations

Magnetic and electric fields are governed by Maxwell's equations. Historically, the four equations known as Maxwell's equations existed as experimental laws, in fragmentary forms, long before him. The laws were combined by Maxwell [1873], who extended the theory and postulated a set of differential equations which apply to all macroscopic electromagnetic phenomena.

In the following,  $\mathbf{E}$  and  $\mathbf{B}$  are the electric and magnetic fields,  $\mathbf{J}$  is the electric current density vector,  $\mathbf{D}$  is the electric displacement, and  $\sigma$ ,  $\mu_0$ ,  $\epsilon_0$  are material constants representing the electrical conductivity of the material, the permeability and permittivity of free space. The first equation, Faraday's law, relates the magnetic field and the electric field at a point in space, stating that changes in time of a magnetic field generate an electric field

$$\frac{\partial \mathbf{B}}{\partial t} = -\nabla \times \mathbf{E}. \quad (2.4)$$

Ampère's law determines the magnetic field associated with an electric current

$$\nabla \times \mathbf{H} = \mathbf{J} + \frac{\partial \mathbf{D}}{\partial t}, \quad (2.5)$$

where  $\mathbf{H}$  is the magnetic field strength, which is related to the magnetic (induction) field through the constitutive relation

$$\mathbf{B} = \mu_0 \mathbf{H}. \quad (2.6)$$

The electric displacement is given by

$$\mathbf{D} = \epsilon_0 \mathbf{E}. \quad (2.7)$$

For low frequencies,  $\partial \mathbf{D} / \partial t$  is significantly smaller than  $\mathbf{J}$  in conductors, even in poor conductors such as the mantle. In addition, if the magnetic permeability is constant throughout the media, (2.5) can be written as

$$\nabla \times \mathbf{B} = \mu_0 \mathbf{J}. \quad (2.8)$$



Since there are no magnetic monopoles, the magnetic field lines are continuous and close onto themselves. Therefore the continuity equation for the magnetic field is

$$\nabla \cdot \mathbf{B} = 0. \quad (2.9)$$

The set of equations is completed by the constitutive equation that relates the electric current to the electric field

$$\mathbf{J} = \sigma \mathbf{E}. \quad (2.10)$$

Like other physical properties, the value of the electric field depends on the frame of reference in which it is measured. In this study, the stationary reference frame of the mantle is assumed.

### 2.3 Potential Fields, Spherical Harmonics and Legendre Functions

The current density  $\mathbf{J}$  in (2.8) is negligible within the mantle and between the surface of the Earth and the ionosphere. From (2.8) it follows that  $\mathbf{B}$  may be taken to be curl-free. This allows the field to be represented as the gradient of a scalar potential

$$\mathbf{B} = -\nabla V. \quad (2.11)$$

In spherical co-ordinates ( $r$  = radius,  $\theta$  = co-latitude,  $\phi$  = longitude) the gradient of a scalar field takes the form

$$\nabla V = \frac{\partial V}{\partial r} \hat{\mathbf{r}} + \frac{1}{r} \frac{\partial V}{\partial \theta} \hat{\boldsymbol{\theta}} + \frac{1}{r \sin \theta} \frac{\partial V}{\partial \phi} \hat{\boldsymbol{\phi}}. \quad (2.12)$$

Combining equations (2.9) and (2.11) yields Laplace's equation

$$\nabla^2 V = 0 \quad (2.13)$$

for the scalar potential  $V$ . Laplace's equation can be written in spherical co-ordinates as

$$\frac{1}{r} \frac{\partial^2 (rV)}{\partial r^2} + \frac{1}{r^2 \sin \theta} \frac{\partial}{\partial \theta} \left( \sin \theta \frac{\partial V}{\partial \theta} \right) + \frac{1}{r^2 \sin^2 \theta} \frac{\partial^2 V}{\partial \phi^2} = 0. \quad (2.14)$$

This equation can be solved using the method of separation of variables, which assumes a solution of the form  $V = R(r)Y(\theta, \phi)$ . Substituting  $R(r)Y(\theta, \phi)$  in (2.14) yields Euler's differential equation for  $R(r)$ , with solutions  $R(r) = r^l$  and  $R(r) = r^{-(l+1)}$ , where  $l(l+1)$  is the separation constant. To represent the magnetic field of internal origin we keep only the solution that vanishes when  $r$  goes to infinity, i.e.,  $R(r) = r^{-(l+1)}$ . The method of separation of variables is applied to find the form of  $Y(\theta, \phi)$ , by assuming that  $Y(\theta, \phi) = P(\theta)E(\phi)$ . This yields Legendre's differential equation for  $P(\theta)$  and a second order ODE for  $E(\phi)$ , with the separation constant  $m^2$ . The solution of the Legendre differential equation has the general form  $P(\theta) = P_{l,m}$ . The  $P_{l,m}$  polynomials are called associated Legendre functions and their general expression is given by

$$P_{l,m}(\mu) = \frac{(1-\mu^2)^{\frac{m}{2}}}{2^l l!} \frac{d^{l+m}}{d\mu^{l+m}} (\mu^2 - 1)^l, \quad (2.15)$$

where  $\mu = \cos \theta$ .

Hence, the general solution for the potential of the magnetic field is

$$V = \sum_{l=1}^{\infty} \sum_{m=-l}^l A_{l,m} r^{-(l+1)} \exp(im\phi) P_{l,m}, \quad (2.16)$$

where  $A_{l,m}$  are complex coefficients. A series representation such as the equation (2.16), is called a spherical harmonic expansion and the quantities  $A_{l,m}$  are called spherical harmonic coefficients, whereas the functions  $Y_{l,m}(\theta, \phi) = \exp(im\phi) P_{l,m}(\cos \theta)$  are called spherical harmonics. In this notation  $l$  is the degree and  $m$  is the order of the spherical harmonic. The term  $l = 0$  and  $m = 0$  corresponds to a magnetic monopole, and is therefore excluded from the expansion to be consistent with (2.9).

## 2.4 Orthogonality of Spherical Harmonics, Schmidt Normalization and Gauss Coefficients

Spherical harmonic functions are orthogonal basis functions for expanding scalar functions on a sphere. The orthogonality condition on the unit sphere is

$$\int_{\Omega} Y_{l,m} Y_{s,t}^* d\Omega = \frac{4\pi(l+m)!}{(2l+1)(l-m)!} \delta_{ls} \delta_{mt}, \quad (2.17)$$

where \* represents complex conjugation and  $d\Omega$  represents the solid angle,  $d\Omega = \sin \theta d\theta d\phi$ . The orthogonality property becomes important when we want to expand a function in a series of spherical harmonics. Applying the orthogonality of spherical harmonics we can determine the amplitude of the expansion coefficients.

The spherical harmonics are often normalized, and several normalizations are used in geomagnetism. Fully normalized  $Y_l^m$  satisfy

$$\int_{\Omega} Y_l^m Y_s^{t*} d\Omega = \delta_{ls} \delta_{mt}. \quad (2.18)$$

The Schmidt quasi-normalized form was introduced by Schmidt [1935] and is the most widely used in geomagnetism. The orthogonality relationship in this case is given by

$$\int_{\Omega} Y_l^m Y_s^{t*} d\Omega = \frac{4\pi}{2l+1} \delta_{ls} \delta_{mt}. \quad (2.19)$$

The relationship between the un-normalized spherical harmonics  $Y_{l,m}$  and the Schmidt normalized spherical harmonics  $Y_l^m$  is

$$Y_l^0 = Y_{l0},$$

$$Y_l^m = \left[ \frac{2(l-m)!}{(l+m)!} \right]^{1/2} Y_{lm}, \quad \text{for } m > 0. \quad (2.20)$$

The Schmidt normalized coefficients are frequently used in the expression of the magnetic potential  $V$  in (2.16). Since the magnetic potential is a real scalar, the expansion of

$V$  in (2.16) can be re-defined in terms of real quantities. It is also customary to multiply the expression by the mean radius of the Earth surface,  $a$ , such that the spherical harmonic coefficients have the same dimension as the field  $\mathbf{B}$ . Re-arranging constants and using the Schmidt normalization for the Legendre functions, the general solution for the potential of the magnetic field of internal origin used almost unanimously is

$$V = a \sum_{l=1}^N \sum_{m=0}^l \left(\frac{a}{r}\right)^{l+1} (g_l^m \cos m\phi + h_l^m \sin m\phi) P_l^m(\cos\theta). \quad (2.21)$$

The coefficients  $g_l^m$  and  $h_l^m$  in this representation are called Gauss coefficients in the honour of the well known mathematician and philosopher Carl Friedrich Gauss, who was the first to employ the spherical harmonic expansion to describe the magnetic potential in 1839.

## 2.5 Vector Spherical Harmonics

As mentioned before, scalar functions on a sphere can be expanded in surface spherical harmonics by exploiting the orthogonality of the basis functions  $Y_l^m$

$$f(\theta, \phi) = \sum_{l=0}^{\infty} \sum_{m=-l}^l A_l^m Y_l^m(\theta, \phi), \quad (2.22)$$

where  $A_l^m$  is a complex constant. The expansion theorem can be extended to vector-valued functions on a spherical surface. The approach relies on representing a vector field in terms of three scalar potentials

$$\mathbf{u} = U \hat{\mathbf{r}} + \nabla_1 V + (-\hat{\mathbf{r}} \times \nabla_1) W, \quad (2.23)$$

where

$$\nabla_1 = \hat{\boldsymbol{\theta}} \frac{\partial}{\partial \theta} (\cdot) + \hat{\boldsymbol{\phi}} \frac{1}{\sin \theta} \frac{\partial}{\partial \phi} (\cdot) \quad (2.24)$$

is the tangential derivative.

The unit radial vector  $\hat{\mathbf{r}}$ , the tangential derivative  $\nabla_1$  and  $(-\hat{\mathbf{r}} \times \nabla_1)$  are orthogonal and determine a vector basis for  $\mathbf{u}$ . The scalar potentials  $U, V, W$  can be expanded in spherical harmonics. Using the definition of vector harmonics

$$\begin{aligned}\mathbf{R}_l^m &= \hat{\mathbf{r}} Y_l^m(\theta, \phi), \\ \mathbf{S}_l^m &= \nabla_1 Y_l^m(\theta, \phi), \\ \mathbf{T}_l^m &= -\hat{\mathbf{r}} \times \nabla_1 Y_l^m(\theta, \phi)\end{aligned}\quad (2.25)$$

the field  $\mathbf{u}$  can be expressed as

$$\mathbf{u} = \sum_{l=0}^{\infty} \sum_{m=-l}^l A_l^m(r) \mathbf{R}_l^m(\theta, \phi) + B_l^m(r) \mathbf{S}_l^m(\theta, \phi) + C_l^m(r) \mathbf{T}_l^m(\theta, \phi). \quad (2.26)$$

The  $\mathbf{S}_l^m$  and  $\mathbf{R}_l^m$  parts are often described as the spheroidal part of the field, whereas  $\mathbf{T}_l^m$  is the toroidal part. In terms of the spherical co-ordinates, the new vector basis can be expressed as

$$\begin{aligned}\mathbf{R}_l^m &= \hat{\mathbf{r}} Y_l^m(\theta, \phi), \\ \mathbf{S}_l^m &= \hat{\theta} \partial_\theta Y_l^m(\theta, \phi) + \hat{\phi} \frac{1}{\sin \theta} \partial_\phi Y_l^m(\theta, \phi), \\ \mathbf{T}_l^m &= \hat{\theta} \frac{1}{\sin \theta} \partial_\phi Y_l^m(\theta, \phi) - \hat{\phi} \partial_\theta Y_l^m(\theta, \phi).\end{aligned}\quad (2.27)$$

When the vector field is solenoidal (i.e.,  $\nabla \cdot \mathbf{u} = 0$ ), an alternative representation for  $\mathbf{u}$  relies on the fact that there are unique scalar fields  $\mathcal{P}$  and  $\tau$  such that

$$\mathbf{u} = \nabla \times \Lambda \mathcal{P} + \Lambda \tau, \quad (2.28)$$

where  $\Lambda = \nabla \times \hat{\mathbf{r}}$ . This representation is very useful since it leads to a great deal of simplification during computations and therefore was often used in this work. The field  $\nabla \times \Lambda \mathcal{P}$  is called the poloidal part of  $\mathbf{u}$ . The field  $\Lambda \tau$  is called the toroidal part of  $\mathbf{u}$ . Using the definition of the vector harmonics, the toroidal and poloidal parts of a field can be written as

$$\nabla \times \hat{\mathbf{r}} \tau = \frac{1}{r} t_{l,m} \mathbf{T}_{l,m}, \quad (2.29)$$

$$\nabla \times \nabla \times \mathcal{P} \hat{\mathbf{r}} = \frac{l(l+1)}{r^2} p_{l,m} \mathbf{R}_l^m + \frac{1}{r} \partial_r \mathbf{S}_l^m. \quad (2.30)$$

The vector spherical harmonics are orthogonal and this property is used to expand vector-valued functions on a sphere. When using the Schmidt normalized Legendre functions, the orthogonality relations for the vector spherical harmonics are:

$$\begin{aligned} \int_0^{2\pi} \int_0^\pi R_l^m R_s^{t*} \sin \theta d\theta d\phi &= \frac{4\pi}{2l+1} \delta_{ls} \delta_{mt}, \\ \int_0^{2\pi} \int_0^\pi S_l^m S_s^{t*} \sin \theta d\theta d\phi &= l(l+1) \frac{4\pi}{2l+1} \delta_{ls} \delta_{mt}, \\ \int_0^{2\pi} \int_0^\pi T_l^m T_s^{t*} \sin \theta d\theta d\phi &= l(l+1) \frac{4\pi}{2l+1} \delta_{ls} \delta_{mt}. \end{aligned} \quad (2.31)$$

## Chapter 3

### THE PROBLEM

#### 3.1 A Conceptual Model

The sediment model of *Buffett et al.* [2000] suggests that solidification of the core causes chemical dis-equilibrium which is restored by precipitation of lighter elements from the liquid core. Deposition of these lighter elements occurs with some initial porosity, but viscous compaction of the layer gradually decreases the porosity and expels the interstitial liquid iron. An important issue is whether the liquid iron remains interconnected in the silicate matrix or if isolated pockets of metallic liquid develop as the porosity decreases. In this study it is assumed that the liquid iron remains interconnected and a layer with variable conductivity develops at the CMB. According to the predictions of the sediment model, silicates tend to accumulate in the topographic highs of the boundary, which can be viewed as basins from the standpoint of the light material in the outer core. As a result of sediment accumulation, these regions exhibit high porosities. The presence of residual liquid iron raises the bulk conductivity of such regions close to core values. In contrast, regions where the boundary is depressed may have no sediments, or sediments with very low porosity because of low accumulation rates. In either case, the solid side of the CMB (including the sediment layer) lacks interstitial iron. In this context, the variable iron content of the silicate layer yields lateral variations in the electrical conductivity (Figure 3.1).

A geodynamic estimate of topography at the CMB is shown in Figure 3.3 b. [*Forte*

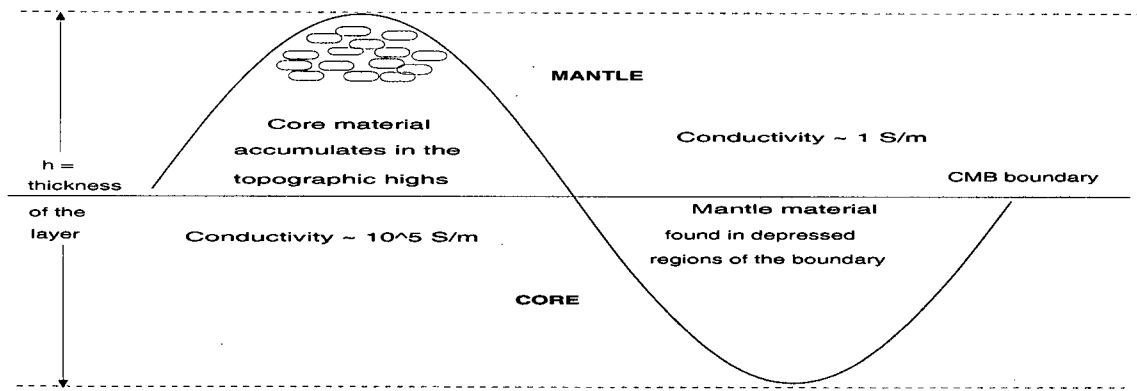


Figure 3.1: Schematic illustration of the thin layer model, showing undulations of the boundary topography. The thickness of the layer,  $h$  is assumed to be 1 km. Conductivities within the layer in regions of topographic highs are assumed to be  $2 \times 10^5$  S/m, whereas the conductivities in depressed regions are 1 S/m.

*et al.*, 1995]. This estimate of CMB topography shows positive radial displacement underneath the Pacific, whereas the boundary in the surrounding regions is displaced towards the core. Since the accumulation of sediments is related to the topography, it is reasonable to assume that the distribution of conductivity emulates the CMB topography. The configuration of the boundary topography is used to devise a model for lateral variations in electrical conductivity at the CMB. The dominant pattern of boundary topography is described in terms of spherical harmonics by the second degree terms, of which the sectoral  $Y_2^2(\theta, \phi)$  term is predominant. The coefficients of the spherical harmonic representation of the conductivity model are assumed to be proportional to the coefficients of *Forte et al.* [1995] topography model. The region under the Pacific becomes anomalously conductive, alternating with low conductivities in the surrounding regions. This choice is based on geodynamic predictions of positive radial displacement of the boundary, but it is also compatible with the detection of the ULVZs.

Estimates for the physical properties of the layer are inferred from the predicted profiles of porosity and electrical conductivity of the sediment model. According to



*Buffett et al.* [2000], the largest porosity in the silicate layer occurs at the interface where the sediments are deposited. The porosity might be as large as 50%, but decreases rapidly with the distance into the sediment layer. Beyond a distance of 1.5 km from the core-sediment interface, the porosity is almost invariant and has a residual value of less than 5% . Hence, the largest volume of interstitial iron occurs over a 1.5 km region adjacent to the sediment interface. Here, the conductivity is expected to be on the order of  $10^5$  S/m.

The conductivity model assumes a sediment layer with a thickness  $h$  of 1 km, and a depth-averaged conductivity  $\sigma$  that varies between 1 and  $2 \times 10^5$  S/m, depending on the geographic position. The spatial distribution of  $\sigma$  is described using the spherical harmonic representation

$$\sigma(\theta, \phi) = \sigma_0 + \sum_{l=1}^{\infty} \sum_{m=0}^l (\sigma_{l,m}^g \cos m \phi + \sigma_{l,m}^h \sin m \phi) P_l^m(\cos \theta), \quad (3.1)$$

where  $\sigma_0$  is the mean value and  $\sigma_{l,m}^g$  and  $\sigma_{l,m}^h$  give the amplitude and phase of the lateral variation of  $\sigma(\theta, \phi)$ . (Schmidt normalization [*Langel*, 1987] is used for the associated Legendre function  $P_l^m$ .) Since the conductivity configuration is proportional to the spherical harmonic representation of the CMB topography of the *Forte et al.* [1995], I have restricted the calculations to the second degree terms of the  $\sigma_{l,m}^g$  and  $\sigma_{l,m}^h$  series, as these have the largest contribution to the topography function. In addition, there is no need to consider the zonal term as it has no longitudinal dependence and therefore does not affect the VGP longitude. Consequently, the following particular configuration is considered for the conductivity model (Figure 3.2)

$$\sigma(\theta, \phi) = \sigma_0 + \sum_{m=1}^2 (\sigma_{2,m}^g \cos m \phi + \sigma_{2,m}^h \sin m \phi) P_2^m(\cos \theta). \quad (3.2)$$

My choice of parameters yields an average conductivity within the layer of order  $10^5$  S/m. This yields a total conductance of order  $10^8$  S, in agreement with the predictions

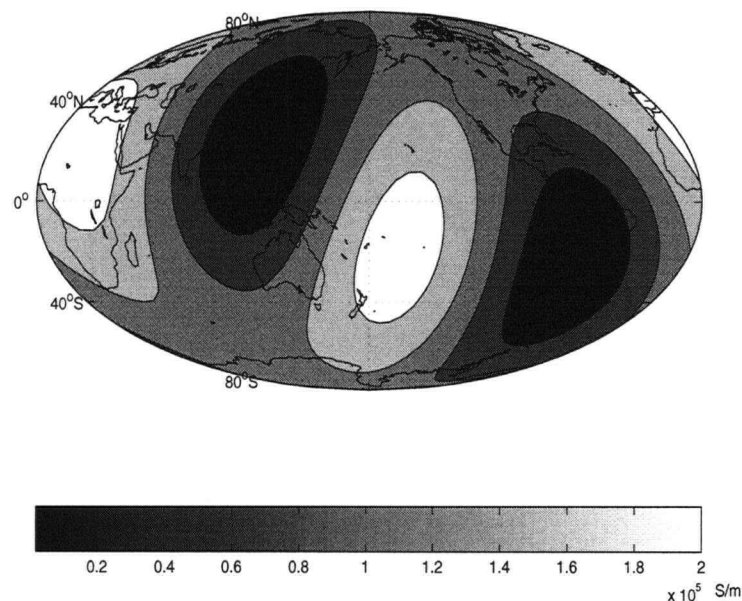


Figure 3.2: The conductivity model (TC) based on the topography of the core-mantle boundary [Forte *et al.*, 1995].

of the sediment model. Is The existence of a conductive region in the lowermost mantle is generally accepted, however, the total conductance of such a region depends on the nature of material transport across the CMB. Several transport processes are thought to contribute to the enrichment in core material of the core-mantle interface. These include the flow of liquid iron through capillary percolation or convective entrainment [Knittle, 1998], transport of core material along grain boundaries [Poirer *et al.*, 1998], and underplating of the CMB by accumulation of lighter core constituents as described by the sediment model of Buffett *et al.* [2000]. Separately, or in combination, these different processes could influence the composition and therefore the conductivity of the lower mantle over distances as large as 100 km [Stevenson, 2003] above the CMB. The total conductance of the lower mantle differs from one model to another. As an example, the model of Poirer *et al.* [1998] predicts a conductance which is several orders of

magnitude lower than the values predicted by the sediment model, but the mechanism of iron infiltrating the mantle through grain wetting differs significantly from the mechanism of sediment accumulation. The difficulty in devising a conductivity model lies in the fact that currently there are few constraints to model the conductivity of the CMB region. Additional constraints on the amplitude and phase of the conductivity model will be inferred later in my study by analyzing the present-day secular variation of the Earth's magnetic field.

The influence of the conductive layer on the magnetic field is studied in the context of a polarity reversal. The transition field models that have been proposed in various studies attempt to relate the mechanism of reversals to the dynamics of the outer core. One model assumes that the dipole disappears during reversals, as suggested by the reduction in remanent magnetization before and after the change in field polarity [*e.g.*, *Opdyke et al.*, 1973; *Gubbins and Sarson*, 1994; *Olson*, 2002]. Other studies suggest that the field retains a primarily dipolar character [*e.g.*, *Creer and Ispir*, 1970; *Hammond et al.*, 1979] and that it reverses not by disappearing or by becoming non-dipolar, but through the rotation of the dipole axis [*Runcorn*, 1992]. Some studies have found evidence that the transitional fields were predominantly characterized by higher-order non-zonal harmonics [*Clement*, 1991; *Hoffman*, 1992], or even zonal, remaining axisymmetric but not dipolar [*Hoffman and Fuller*, 1978; *Fuller et al.*, 1979]. In this work, the polarity transition is modelled by assuming that the axial dipole field decreases in intensity to zero and increases gradually in the opposite direction. The Gauss coefficient  $g_1^0$ , which defines the axial dipole, decays to zero and builds up in the opposite direction, at a prescribed rate. The non-dipole terms are stationary for the duration of one reversal and are determined from a statistical field model [*Constable and Parker*, 1988]. The duration of the reversal is typically a few thousand years. The model I adopted for the transition field relies on observations of secular variation of the internal field, which reveal a precipitous decline

in the dipole over the past 150 years. This decrease could eventually lead to a reversal, having the same characteristics with the last known reversal [*Hulot et al.*, 2002].

### 3.2 Formulation of the Problem

Temporal variations in the axial dipole induce an electric field in the layer, which generates electric currents in the conductive parts of the layer. Circulation of currents within the layer generates a secondary magnetic field which perturbs the total field. Calculations of the secondary field are used to evaluate the VGP paths and to assess whether the amplitude of the perturbation is sufficient to rise above the natural variability in the non-dipole field, thereby leaving its signature on the VGP paths.

Magnetic and electric fields inside and above the conductive layer are governed by Maxwell's equations in a low frequency approximation [*Gubbins and Roberts*, 1987] described in the previous chapter. The time derivative of the axial dipole in (2.4) is estimated by assuming that the axial dipole decays and grows in the opposite direction over the time interval of a reversal. It is also assumed that the initial and final amplitude of the dipole equals the present-day value.

Using an imposed value for  $\partial \mathbf{B} / \partial t$  at the CMB, (2.4) is solved for the electric field  $\mathbf{E}$  and the current  $\mathbf{J}$  in the layer is later determined from (2.10). Finally, the current  $\mathbf{J}$  in (2.8) is used to solve for a secondary magnetic field  $\tilde{\mathbf{B}}$ , whose effect is added to the magnetic field of core origin. The method of solving for the secondary field  $\tilde{\mathbf{B}}$  uses a thin sheet approximation. Temporal fluctuations in the axial dipole during a reversal are probably very complicated, but for the purpose of predicting VGP paths the model assumes that the rate of change of the dipole is constant. Hence, both  $\mathbf{E}$  and  $\tilde{\mathbf{B}}$  in the layer are independent of time. The absence of temporal variations in  $\tilde{\mathbf{B}}$  means that the variation on the left-hand side of (2.4) is due solely to changes in the dipole. As a

consequence, the electric field  $\mathbf{E}$  is not altered by the generation of secondary field  $\tilde{\mathbf{B}}$ .

### 3.3 Boundary Conditions

The boundary conditions on  $\mathbf{B}$  and  $\mathbf{J}$  are derived by considering the behaviour of the magnetic field at an interface between two media of different, but finite electrical conductivities. Let  $\hat{\mathbf{n}}$  be the normal to the interface. Integrating the solenoidal condition (2.9) throughout a small volume, shows that  $\mathbf{B} \cdot \hat{\mathbf{n}}$  is continuous. Likewise, applying the divergence operator on (2.8) leads to the solenoidal condition on  $\mathbf{J}$  (*i.e.*,  $\nabla \cdot \mathbf{J} = 0$ ), which implies that  $\mathbf{J} \cdot \hat{\mathbf{n}}$  must be continuous. Applying Stokes' theorem in (2.4) indicates that the tangential component of the electric field  $\mathbf{E} \cdot \hat{\mathbf{t}}$  is also continuous across the boundary. Gauss' law

$$\nabla \cdot \mathbf{E} = \frac{1}{\epsilon_0} \Sigma, \quad (3.3)$$

where  $\epsilon_0$  is the electric permittivity of free space and  $\Sigma$  is the electric charge density, shows that  $\mathbf{E} \cdot \hat{\mathbf{n}}$  is discontinuous if a charge develops. This discontinuity is also indicated by Ohm's law (2.10): if  $\mathbf{J} \cdot \hat{\mathbf{n}}$  is continuous, but  $\sigma$  is not, then  $\mathbf{E} \cdot \hat{\mathbf{n}}$  must be discontinuous.

To determine the boundary condition on the tangential component of the magnetic field, consider a small volume that encloses a portion of the interface. Applying Stokes' theorem to (2.8) for a rectangular surface perpendicular to the interface layer and making the height of the rectangle infinitesimally small, shows that  $\mathbf{B} \cdot \hat{\mathbf{t}}$  is discontinuous across the boundary.

All these conditions can be summarized as follows:

$$[\mathbf{B}]_{-}^{+} \cdot \hat{\mathbf{n}} = 0$$

$$[\mathbf{J}]_{-}^{+} \cdot \hat{\mathbf{n}} = 0$$

$$[\mathbf{E}]_{-}^{+} \cdot \hat{\mathbf{t}} = 0$$

$$[\mathbf{E}]_{-}^{+} \cdot \hat{\mathbf{n}} \neq 0$$

$$[\mathbf{B}]_{-}^{+} \cdot \hat{\mathbf{t}} \neq 0,$$

where  $[\ ]_{-}^{+}$  denotes the jump across the interface. The continuity of the normal (radial) component of the magnetic field is used to match the field outside the layer when one medium is an insulator (*i.e.*, mantle).

### 3.4 Calculation of the Electric Current in the Layer

The solenoidal condition in (2.9) means that  $\mathbf{B}$  can be expressed in terms of a vector potential. Hence, the dipole part of the field is represented as

$$\mathbf{B}_1^0 = \nabla \times \mathbf{A}. \quad (3.4)$$

Substituting  $\mathbf{B}_1^0$  in (2.4) and interchanging the order of differentiation we get

$$\nabla \times \frac{\partial \mathbf{A}}{\partial t} = -\nabla \times \mathbf{E},$$

and further

$$\nabla \times \left[ \frac{\partial \mathbf{A}}{\partial t} + \mathbf{E} \right] = 0.$$

The quantity between brackets is irrotational, thus conservative, so it can be written as the gradient of a scalar potential

$$\frac{\partial \mathbf{A}}{\partial t} + \mathbf{E} = -\nabla \phi, \quad (3.5)$$

where  $\phi$  is an arbitrary scalar. The solution for the electric field is then

$$\mathbf{E} = -\frac{\partial \mathbf{A}}{\partial t} - \nabla \phi. \quad (3.6)$$

In the previous chapter it has been shown that the magnetic field can be decomposed into poloidal and toroidal parts (2.28). Because the axial dipole  $\mathbf{B}_1^0$  is purely poloidal,

let

$$\mathbf{B}_1^0 = \nabla \times \nabla \times (\mathcal{P}\hat{\mathbf{r}}), \quad (3.7)$$

where  $\mathcal{P}$  is a poloidal scalar given by  $\mathcal{P} = p_1^0 Y_1^0$ . Equating (3.7) and (2.11) gives the relation between the coefficient of  $\mathcal{P}$  and the corresponding Gauss coefficient

$$p_1^0 = \frac{a^3}{r} g_1^0. \quad (3.8)$$

At the Earth's surface,  $\mathcal{P} = a^2 g_1^0 \cos \theta$ . The vector potential  $\mathbf{A}$  is found by equating  $\mathbf{B}_1^0$  from (3.7) and (3.4)

$$\mathbf{A} = \nabla \times (\mathcal{P}\hat{\mathbf{r}}). \quad (3.9)$$

Substituting  $\mathbf{A}$  in (3.6) we get

$$\mathbf{E} = -\nabla \times (\dot{\mathcal{P}}\hat{\mathbf{r}}) - \nabla \phi, \quad (3.10)$$

where the dot represents differentiation with respect to time.

Ohm's Law (2.10) yields the density current in the layer

$$\mathbf{J} = -\sigma \nabla \times (\dot{\mathcal{P}}\hat{\mathbf{r}}) - \sigma \nabla \phi, \quad (3.11)$$

responsible for the secondary field  $\tilde{\mathbf{B}}$ . The scalar  $\dot{\mathcal{P}}$  depends on the rate of change of the dipole field and is treated as a known parameter. Therefore the term  $-\sigma \nabla \times (\dot{\mathcal{P}}\hat{\mathbf{r}})$  is readily computed while the current due to the potential  $\phi$  remains to be determined. The term  $\sigma \nabla \phi$  is evaluated by imposing the condition that the electric charge is conserved

$$\nabla \cdot \mathbf{J} = 0. \quad (3.12)$$

Substituting (3.11) into (3.12) and applying vector identities yields

$$(\nabla \sigma) \cdot \nabla \times (\dot{\mathcal{P}}\hat{\mathbf{r}}) = -\nabla \cdot \sigma \nabla \phi. \quad (3.13)$$

The term  $\sigma \nabla \phi$  can be directly determined from (3.13). Since our interest lies mainly in the current  $\sigma \nabla \phi$ , this is a faster approach than to compute the potential  $\phi$  and then determine the current due to this potential.

To do this, we first compute the left hand side of (3.13). Since the  $\nabla \times (\dot{\mathcal{P}} \hat{\mathbf{r}})$  has only a  $\hat{\phi}$  component, we only consider the  $\hat{\phi}$  component of the conductivity gradient in evaluating the dot product on the left hand side of (3.13). The resulting scalar has a spherical harmonic expansion which is identical to that of the conductivity distribution. For instance, a lateral variation in  $\sigma$  with a  $Y_2^2(\theta, \phi)$  term gives

$$(\nabla \sigma) \cdot \nabla \times (\dot{\mathcal{P}} \hat{\mathbf{r}}) = \frac{2a^3}{r^3} g_1^0 (\sigma_{2,2}^h \cos m\phi - \sigma_{2,2}^g \sin m\phi) P_2^2(\cos \theta). \quad (3.14)$$

A similar result is obtained with a distribution of conductivity that varies as  $Y_2^1(\theta, \phi)$ . It is important to note here that the spherical harmonic correspondence between  $\sigma$  and the left-hand side of (3.13) is only possible because the poloidal scalar  $\dot{\mathcal{P}}$  represents the axial dipole, with  $l = 1$  and  $m = 0$ .

The spherical harmonic representation of  $(\nabla \sigma) \cdot \nabla \times (\dot{\mathcal{P}} \hat{\mathbf{r}})$  establishes the form of the potential  $\phi$ . Because  $(\nabla \sigma) \cdot \nabla \times (\dot{\mathcal{P}} \hat{\mathbf{r}})$  has the same angular order as  $\sigma$ , and this order must equal the sum of the angular orders of  $\sigma$  and  $\phi$ , by virtue of orthogonality of the spherical harmonics  $\phi$  must be zonal (*i.e.*, with angular order  $m = 0$ ). Since  $\phi$  has no longitudinal dependence, the gradient  $\nabla \phi$ , evaluated as in (2.12), has only a  $\hat{\theta}$  component. Let now

$$\sigma \nabla \phi = f_\theta \hat{\theta}. \quad (3.15)$$

We can evaluate  $f_\theta$  by substituting (3.15) into (3.13), which gives

$$\frac{1}{r \sin \theta} \frac{\partial}{\partial \theta} (\sin \theta f_\theta) = -(\nabla \sigma) \cdot \nabla \times (\dot{\mathcal{P}} \hat{\mathbf{r}}). \quad (3.16)$$

Multiplying (3.16) by  $(r \sin \theta)$  and integrating with respect to  $\theta$  determines  $f_\theta$  (and hence  $\sigma \nabla \phi$ ).



As an example, when  $(\nabla\sigma) \cdot \nabla \times (\hat{P}\hat{r})$  has a  $Y_2^2$  dependence, the integral over  $\theta$  in the right hand side of (3.16) has the form

$$F(\theta) \equiv \int P_2^2(\cos\theta) \sin\theta d\theta = \frac{\sqrt{6}}{4} \frac{\cos^3\theta}{3} - \frac{\sqrt{6}}{4} \cos\theta + C, \quad (3.17)$$

where the value of  $C$  is chosen to ensure that  $\sigma\nabla\phi$  vanishes at the poles. Expressing  $f_\theta$  in terms of  $F(\theta)$  gives

$$f_\theta = \frac{2a^3}{r^2} \dot{g}_1^0 (\sigma_{2,2}^h \cos 2\phi - \sigma_{2,2}^g \sin 2\phi) \frac{F(\theta)}{\sin\theta}. \quad (3.18)$$

The total electric current  $\mathbf{J}$ , computed as above from (3.11) has the form

$$\mathbf{J} = \frac{2a^3}{r^2} \dot{g}_1^0 \left[ (\sigma_{2,2}^h \cos 2\phi - \sigma_{2,2}^g \sin 2\phi) \frac{F(\theta)}{\sin\theta} \hat{\theta} - (\sigma_{2,2}^g \cos 2\phi + \sigma_{2,2}^h \sin 2\phi) \sin\theta \hat{\phi} \right]. \quad (3.19)$$

A similar treatment is used to compute the potential term and later the total electric current when the conductivity distribution varies as  $Y_2^1$ .

The magnetic field generated by the current  $\mathbf{J}$  is computed from (2.8), *i.e.*,  $\nabla \times \mathbf{B} = \mu_0 \mathbf{J}$ . The poloidal part of the magnetic field is associated with toroidal electric currents, whereas the toroidal part is related to poloidal currents in the layer. At the Earth's surface we are able to measure only the poloidal part of the magnetic field, and although a toroidal field may be generated in the layer due to poloidal currents, it cannot contribute to the VGP paths. We confine our attention to the part of the current  $\mathbf{J}$  that contributes to the magnetic potential field at the surface, which is associated with the toroidal vector harmonic, defined by (2.29). The toroidal part of  $\mathbf{J}$  is decomposed into spherical harmonic components

$$\mathbf{J}_T = \sum_{l=1}^{\infty} \sum_{m=0}^l j_l^m \mathbf{T}_l^m, \quad (3.20)$$

where the coefficients  $j_l^m$  are evaluated using the orthogonality property of the vector harmonics (2.31). The first non-zero coefficient of the expansion of  $\mathbf{J}$  is found to be  $j_3^2$

when  $\sigma$  has a  $Y_2^2$  dependence, and  $j_1^1$  when  $\sigma$  has a  $Y_2^1$  dependence. Terms with higher order  $l$  cause magnetic perturbations which are more rapidly attenuated by the upward continuation to the surface and contribute much less to the VGP paths.

So far we have determined the horizontal current which arises in the conductive layer from the time variation of the axial dipole. Secular variation models of the geomagnetic field show that the equatorial dipole component may also vary with time during a reversal. This component is represented by the terms  $g_1^1$  and  $h_1^1$  for the spherical expansion of  $V$  in (2.21). To determine the electric current which arises from the variation of the equatorial dipole, the development of the equations is the same as before and the current is still given by (3.11), but now since the equatorial dipole has a latitude and longitude dependence, the poloidal scalar  $\mathcal{P}$  is given by  $\mathcal{P} = p_1^1 Y_1^1 + \text{complex conjugate}$ . Similar calculation as in the vertical dipole case gives the expression for the real coefficients of the poloidal scalar in terms of Gauss coefficients:

$$\begin{aligned} p_{11}^g &= \frac{a^3}{r} g_1^1 \\ p_{11}^h &= \frac{a^3}{r} h_1^1. \end{aligned} \quad (3.21)$$

With these notations,  $\mathcal{P}$  at the Earth's surface becomes  $\mathcal{P} = \frac{a^2}{\sqrt{2}} (g_1^1 \cos \phi + h_1^1 \sin \phi) \sin \theta$ . In this case,  $\mathcal{P}$  has a more complicated form than that for the axial dipole and therefore the determination of the current is slightly different as we cannot determine directly the term  $\sigma \nabla \phi$  from the current conservation equation (3.13). The calculations get a little bit tedious when it comes to evaluating the potential  $\phi$ . As previously, the toroidal part of the current is decomposed into spherical harmonic components. The lowest harmonics for the electric current generated by the variation of the equatorial dipole are  $Y_2^1$  and  $Y_3^1$ . These terms have smaller amplitudes than those in the previous case because the rate of change for the equatorial dipole is smaller than the rate of change for the axial dipole ( $\dot{g}_1^1 = 15 \text{ nT/y}$  and  $\dot{h}_1^1 = 35 \text{ nT/y}$ ). As a consequence, the contribution of these terms to

the current  $\mathbf{J}$  can be ignored and was not incorporated in further calculations.

### 3.5 Solution for the Magnetic Perturbation Using a Thin Sheet Approximation

The presence of the electric current in the conductive parts of the layer induces a secondary magnetic field which superimposes on top of the existing field. The method of solving for the secondary field  $\tilde{\mathbf{B}}$  uses a thin sheet approximation because the time scale for magnetic diffusion throughout the layer is short compared with the duration of a reversal. The time delay introduced by the electrically conductive layer is given by the diffusion time of the magnetic field in the layer

$$t_d \sim \frac{d^2}{\eta_m} \sim d^2 \mu_0 \sigma, \quad (3.22)$$

where  $d$  represents a scale of the conductive layer and  $\eta_m$  is the magnetic diffusivity. For a layer with a thickness of  $10^3$  m and a conductivity of  $10^5$  S/m, the characteristic decay time is roughly three days. Since the reversal time is a few thousand years, a time delay of three days introduced by the conductive layer is not important in calculating the field  $\tilde{\mathbf{B}}$ . Therefore, it can be safely assumed that the rate of change of the dipole in the layer is given by the downward continuation of the rate of change of the dipole at the surface. Another reason to use the thin layer approximation derives from the fact that the thickness of the layer is three orders of magnitude smaller than the thickness of the overlying mantle. Consequently, the solution to (2.8) for the field at the surface should not depend on the radial distribution of  $\mathbf{J}$  inside the layer.

To determine the secondary magnetic field produced by  $\mathbf{J}$  in the layer, (2.8) is integrated over the volume of a small pill box constructed to contain the thin layer. The upper and lower surfaces of the box coincide with the surfaces of the mantle and core

respectively. The integral

$$\int_V (\nabla \times \tilde{\mathbf{B}}) dV = \mu_0 \int_V \mathbf{J} dV \quad (3.23)$$

is transformed using Gauss' theorem to give

$$\int_S \hat{\mathbf{n}} \times \tilde{\mathbf{B}} dS = \mu_0 \int_V \mathbf{J} dV, \quad (3.24)$$

where  $\hat{\mathbf{n}}$  represents the (outward) normal to the surface of the pill box and  $dS$  indicates the surface element. If the height  $h$  of the pill box becomes vanishingly small, the sides of the pill box contribute nothing to the surface integral, so the only contributions are due to the area of the top  $S^+$  and bottom  $S^-$  of the pill box. Combining the two contributions into a single integral, where  $\hat{\mathbf{r}}$  is the outward normal on the top surface and  $-\hat{\mathbf{r}}$  is the outward normal on the bottom surface, we obtain

$$\int_{S^+} (\hat{\mathbf{r}} \times \mathbf{B}^+ - \hat{\mathbf{r}} \times \mathbf{B}^-) dS = \mu_0 h \int_{S^+} \mathbf{J} dS, \quad (3.25)$$

where the notations  $\mathbf{B}^+, \mathbf{B}^-$  indicate the magnetic fields on the top and bottom of the conductive layer. The RHS of (3.25) is a consequence of assuming that the current  $\mathbf{J}$  does not vary radially, hence the approximation  $dV \sim h dS$  may be used. Because (3.25) is valid for an arbitrary surface area, the integrands are equated to obtain

$$\hat{\mathbf{r}} \times (\mathbf{B}^+ - \mathbf{B}^-) = \mu_0 h \mathbf{J}. \quad (3.26)$$

The region above the layer (*i.e.*, the mantle) can be regarded as poor conductor [Gubbins and Roberts, 1987], sufficiently poor so that  $\nabla \times \mathbf{B}$  is effectively zero. Hence, the magnetic field within the mantle  $\mathbf{B}^+$  is a potential field, described by a potential with radial solution  $r^{-(l+1)}$ . For the magnetic field  $\mathbf{B}^-$  below the conductive layer (*i.e.*, within the core), there are two bounding cases. In one case it is assumed the core is a perfect conductor. This means that the magnetic field at the top of the core is a few orders of magnitude stronger than the field generated in the layer, therefore the magnetic

perturbation does not diffuse into the core and  $\mathbf{B}^- = 0$  in (3.26). The other bounding case treats the core as a perfect insulator. In this case the magnetic field in the core is described by a magnetic potential (with radial dependence  $r^l$ ). The amplitude of the perturbation in the case of a perfectly insulating core is approximately 50% less than that for the perfectly conducting core. However, calculations show that for this value the perturbation does not alter the VGP paths. Hereafter the case of the perfectly conducting core is discussed.

The field above and below the layer must satisfy the boundary condition in (3.26). In the case of a perfectly conducting core, (3.26) reduces to

$$\hat{\mathbf{r}} \times \mathbf{B}^+ = \mu_0 h \mathbf{J}, \quad (3.27)$$

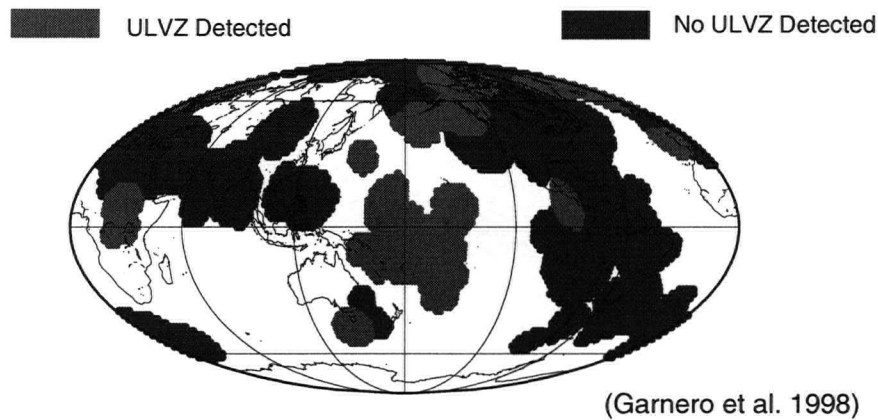
where  $\mathbf{B}^+ = -\nabla \tilde{\Phi}$ . The series representation (2.21) is employed to describe the potential  $\tilde{\Phi}$  by introducing the Gauss coefficients  $\tilde{g}_l^m$  and  $\tilde{h}_l^m$ . By the virtue of the orthogonality of the spherical harmonics, the coefficients  $j_l^m$  of the toroidal current  $\mathbf{J}$  determine the Gauss coefficients  $\tilde{g}_l^m$  and  $\tilde{h}_l^m$  with the same degree and order. The coefficients  $\tilde{g}_l^m$  and  $\tilde{h}_l^m$  are evaluated using (3.27) and upward continued to the surface to obtain

$$\begin{aligned} \tilde{g}_l^m &= N_l^m \left( \frac{b}{a} \right)^{l-1} b \mu h \dot{g}_1^0 \sigma_{2,m}^g, \\ \tilde{h}_l^m &= N_l^m \left( \frac{b}{a} \right)^{l-1} b \mu h \dot{g}_1^0 \sigma_{2,m}^h, \end{aligned} \quad (3.28)$$

where  $b$  is the core radius and  $N_l^m$  is a constant depending on the degree and order of the Gauss coefficient. To give an order of magnitude estimate of the coefficients I assume a present-day dipole that reverses in one thousand years and a 1 km thick layer with a conductivity variation of order  $10^5$  S/m. The largest coefficients in the potential field are at  $l = 3, m = 2$  and  $l = 1, m = 1$  and have amplitudes of roughly several hundred nT. The coefficients of  $\tilde{\Phi}$  in (3.28) are used to generate synthetic data by evaluating the magnetic field components in different locations on the Earth's surface. The components

of the magnetic perturbation are added to the field of core origin to predict the declination and inclination at each site.

## Ultra Low Velocity Zones



## CMB Topography

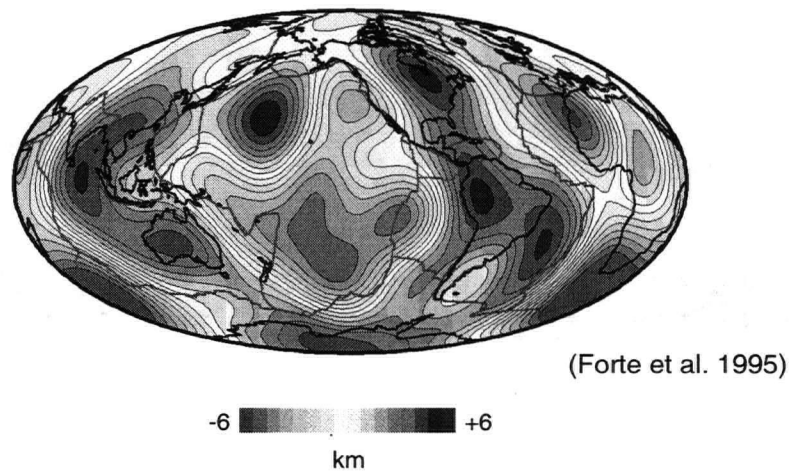


Figure 3.3: **Top:** Location of ultra-low velocity zones (ULVZ) at the core-mantle boundary. **Bottom:** Core-mantle topography inferred from geodynamical calculations. Negative values indicate positive radial displacement of core material into the mantle, positive values indicate regions where the boundary is pushed towards the core.

## Chapter 4

### CONDUCTIVITY MODELS AND RESULTS

#### 4.1 VGP Paths Based on CMB Topography

To determine the influence of the perturbation field on VGP paths, I start with a very simple reversal field in which the axial dipole decays close to zero from its present value and grows in the opposite direction in one thousand years. The variation in time of the axial dipole induces a magnetic perturbation due to the lateral conductivity at the CMB. The conductivity model in Figure 3.2 is devised using the coefficients of order  $l = 2$  of the *Forte et al.* [1995] topography model, since these coefficients are the highest. The term with equatorial symmetry  $l = 2, m = 0$  is not considered as this term does not alter the VGP paths. The  $Y_2^1$  and  $Y_2^2$  terms in the conductivity model  $\sigma$  are responsible for generating the magnetic perturbation, which can be represented at the surface by the potential  $\tilde{\Phi}$ . As shown earlier, the leading terms of  $\tilde{\Phi}$  are described by the  $Y_1^1$  and  $Y_3^2$  Gauss coefficients.

The model is used to calculate the synthetic VGP paths for 500 sites randomly distributed over the Earth's surface (Figure 4.1). The magnetic inclination and declination at each site are calculated from the superposition of the axial dipole and the magnetic perturbation due to  $\tilde{\Phi}$ . I compute the histogram of the VGP paths by binning the results into intervals that span  $20^\circ$  of longitude. To gain a better understanding of the effect of different components of the perturbation on VGP positions, it is instructive to consider the influence of the  $Y_2^1$  and  $Y_2^2$  terms of the conductivity function separately.



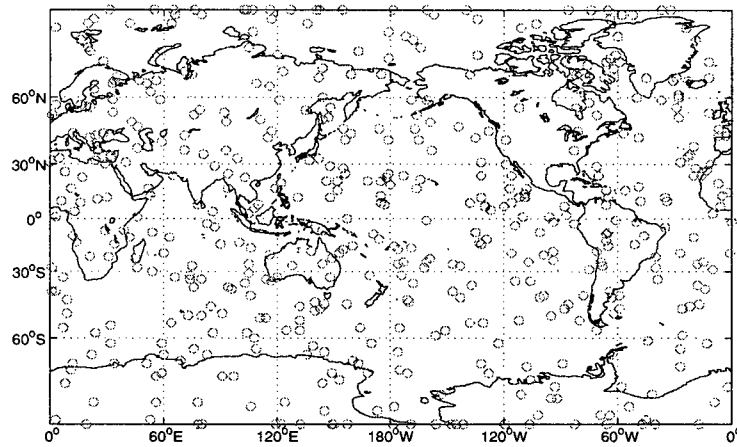


Figure 4.1: The VGP paths have been computed for a random distribution of 500 sites.

The perturbation given by the  $Y_2^1$  part of the conductivity  $\sigma$  is defined by the  $\tilde{g}_1^1$  and  $\tilde{h}_1^1$  coefficients. If taken alone, this part of the perturbation yields VGP paths which concentrate in one single path around  $320^\circ$  ( $40^\circ$ W). This result is expected, because the perturbation describes an equatorial dipole. Consequently the superposition of the axial dipole and the perturbation is a purely dipolar field, so the orientation of the VGP at any location is identical to the dipole orientation. When the  $Y_2^2$  part of  $\sigma$  is considered, the field is composed of the axial dipole and a non-dipole part described by the  $\tilde{g}_3^2$  and  $\tilde{h}_3^2$  coefficients. The histogram of VGP longitudes computed for this field reveals four preferred paths, two of them lying on American and Asian longitudes and two covering mid-Pacific and Western African longitudes (Figure 4.2 top). The result is encouraging because these paths coincide with the observations. Besides the two well-known Asian and American paths, the other two paths have also been encountered in the paleomagnetic database, though in a much smaller number of records [Herrero-Bervera *et al.*, 1987; Liddicoat, 1982].

When the two effects are added together, the non-axial-dipole field is composed of the

coefficients  $\tilde{g}_1^1$ ,  $\tilde{h}_1^1$ ,  $\tilde{g}_3^2$  and  $\tilde{h}_3^2$ . Superposition of these components causes most of the VGP paths to fall on American and Greenland longitudes (Figure 4.2 bottom). More than half of the total number of paths fall in the Eastern region of North America. This result is reminiscent of studies that show more frequent paths over the Americas compared with the Asian paths [e.g., *Tric et al.*, 1991; *Aurnou et al.*, 1996]. The prevalence of the paths through Eastern parts of North America in my results is due to the size of the equatorial dipole terms  $\tilde{g}_1^1$  and  $\tilde{h}_1^1$  relative to the non-dipole terms  $\tilde{g}_3^2$  and  $\tilde{h}_3^2$ . Even though the  $Y_2^1$  part of the conductivity configuration  $\sigma$  contributes less to the total conductivity than the  $Y_2^2$  part (the  $Y_1^1$  part is about 25% of the total), the coefficients  $\tilde{g}_1^1$  and  $\tilde{h}_1^1$  are larger because they represent a longer wavelength field and are attenuated less by upward continuation.

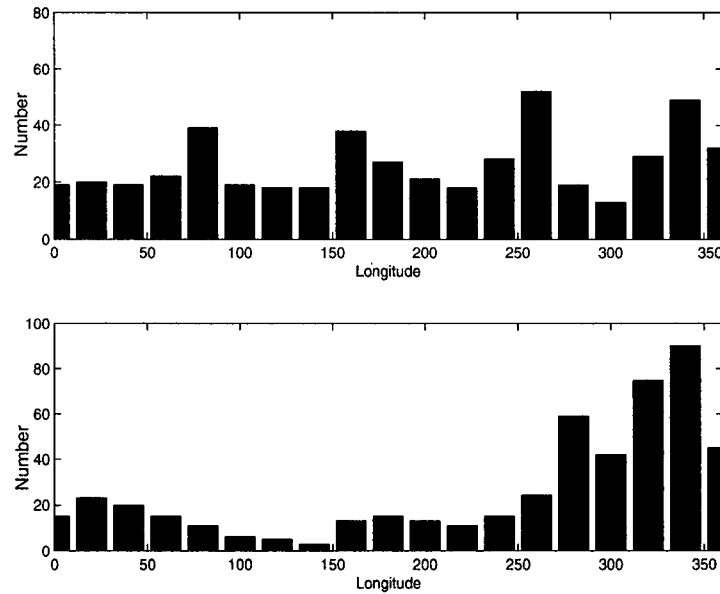


Figure 4.2: **Top:** VGP paths obtained for a field which contains the axial dipole and the  $Y_3^2$  part of the perturbation. **Bottom:** VGP paths obtained when adding the  $Y_1^1$  part of the perturbation to the above field.

The results obtained so far show that the magnetic perturbation induced in the layer can affect the VGP paths during the reversal of the axial dipole. The model yields the preferred paths through America, partially resolving the observations. However, these paths are slightly shifted from the preferred American paths given by the observations. One possible interpretation is that the geographical confinement of the VGP during a reversal is caused by a perturbation field with a slightly different geometry. As seen from the analytic solution, the degree and order of the Gauss coefficients of the perturbed field are functions of the degree and order of both the time-varying magnetic components and conductivity geometry (see Equation 3.28).

A different geometry of the perturbation field can be related to the distribution of the conductivity at the CMB. As shown at the beginning of this section, higher order terms have a very small contribution to the topography function, therefore they were not incorporated in the conductivity model. The feature that could make a difference in the geometry of the VGP paths is the conductivity pattern given by order  $l = 2$  terms. In the following, I attempt to derive new constraints for the phase and amplitude of the conductivity model using the secular variation (SV) data. As seen later, the new constraints yield a model which produces a better agreement between the observed and predicted VGP paths.

## 4.2 Observational Constraints on the Conductivity Model

Decreases in the dipole field induce a secondary magnetic field in the conductive layer at the CMB. The magnetic potential of the perturbation is described at the Earth's surface primarily by the  $Y_3^2$  and  $Y_1^1$  terms, and these terms are well constrained in the present-day field. Historical records over the last hundred years show that the amplitude of the axial dipole is decreasing at a rate which is comparable to the value assumed in

modelling the magnetic polarity reversal.

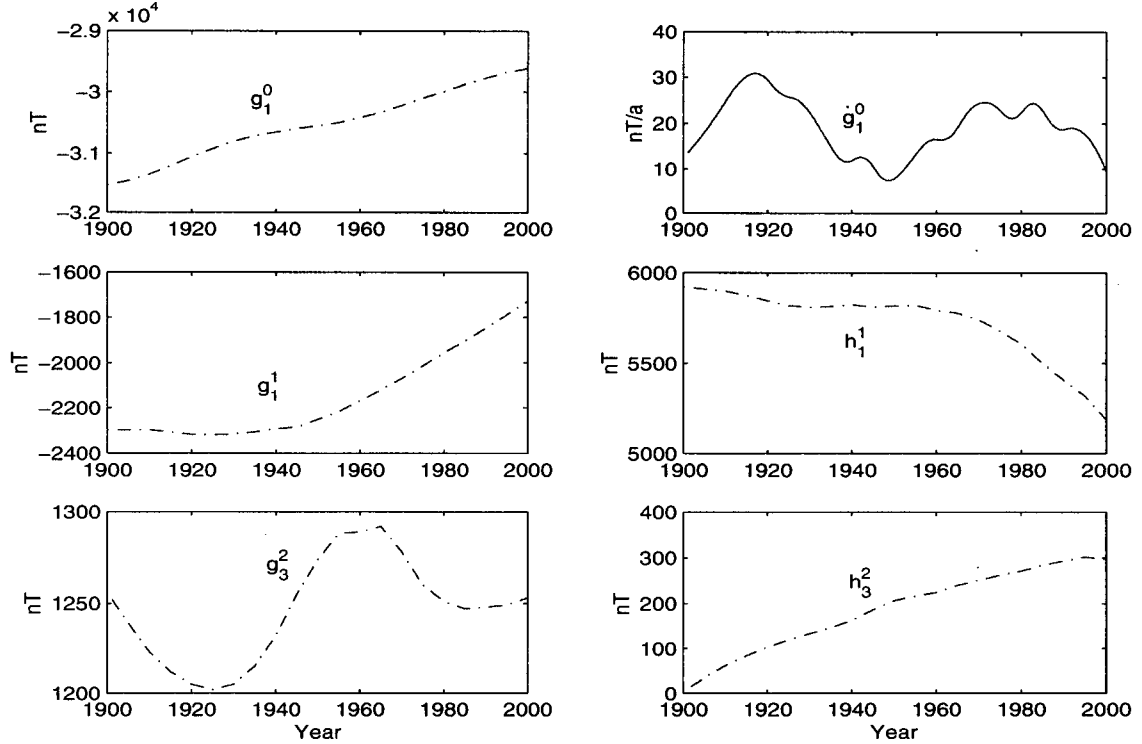


Figure 4.3: Secular variation of the geomagnetic field - IGRF [Langel, 1992]. These observations have been used to derive new constraints on the conductivity model.

Whether the present rate of decay of the dipole is representing an early stage of a reversal or excursion is uncertain at this moment [Hulot *et al.*, 2002; Olson, 2002]. Nevertheless, at this rate of decrease we might expect to see evidence of the perturbation  $\tilde{\Phi}$ , and hence of the layer, in the secular variation observations. Therefore, I attempt to derive constraints for the conductivity model using modern observations.

To constrain the conductivity model, I use the International Geomagnetic Reference Field (IGRF) [Langel, 1992] which describes the secular variation of the magnetic field over the last century (Figure 4.3). The variations that provide the most information on the presence of the conductive layer at the CMB occur in the  $Y_3^2$  and  $Y_1^1$  Gauss

coefficients. I compute the rate of change of the axial dipole from the IGRF model and use this value as input in (3.28) to predict the coefficients of the perturbed potential  $\tilde{\Phi}$ . It is important to note that a constant rate of decrease in the axial dipole causes constant perturbations in the  $Y_3^2$  and  $Y_1^1$  parts of the field, which would be difficult to distinguish from the direct contributions due to the geodynamo. However, fluctuations in the rate of change of the dipole decrease (see Figure 4.3) cause fluctuations in the  $Y_3^2$  and  $Y_1^1$  terms of the magnetic perturbation, which might be identified in the secular variation of the field. The model previously developed to predict the Gauss coefficients of the perturbation field is not entirely valid for the subsequent analysis, since the input  $\partial\mathbf{B}/\partial t$  in (2.4) is no longer constant in time. This fluctuation will contribute to  $\partial\mathbf{B}/\partial t$  in (2.4), so we can no longer assume that the electric field is due solely to changes in the axial dipole. However, the time variations in the magnetic perturbation do not directly contribute to the  $Y_3^2$  and  $Y_1^1$  parts of the potential field at the surface, so my simplified model produces a good approximation for the perturbed coefficients. The goal is to assess whether the predicted fluctuations are evident in the IGRF coefficients and if this provides additional constraints on the structure of the conducting layer at the CMB. I assume that the magnetic field at the surface includes a large contribution from the interior of the core due to the geodynamo and a smaller contribution from the magnetic induction in the conducting layer at the base of the mantle. Since we are looking for evidence of the conducting layer in the fluctuations of the geomagnetic field, it is reasonable to remove the mean from the IGRF coefficients.

I first refer to the non-zonal octupole field coefficients. Figures 4.4 and 4.5 show a comparison of the observed variations in the Gauss coefficients with the predicted variations caused by the observed non-constant decrease in the dipole field. To facilitate comparison of these variations on the same scale, the mean is removed from both the observations and the predictions.

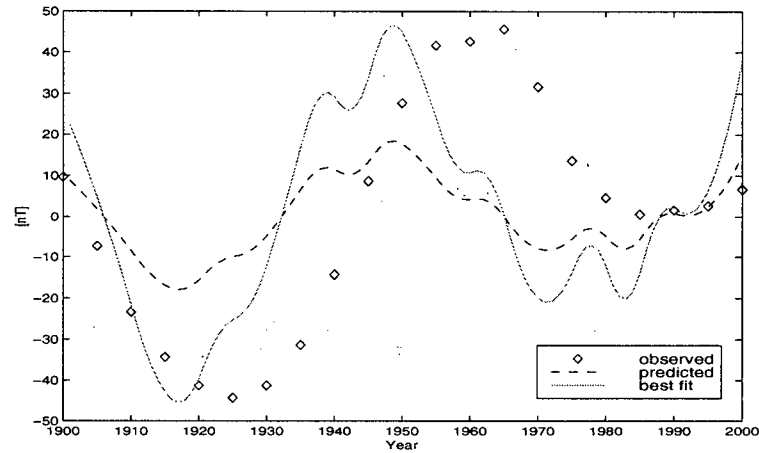


Figure 4.4: Comparison between the observed variations in  $g_3^2$  Gauss coefficients [IGRF, *Langel*, 1992] and predicted variations caused by the fluctuations in the axial dipole field.

The dashed line represents the predictions obtained using the conductivity model based on the CMB topography of *Forte et al.* [1995]. I subsequently refer to this model as the TC model (standing for the topography-based conductivity). We see that the amplitude of the predicted fluctuation in  $g_3^2$  is somewhat smaller than the amplitude of the observed fluctuation. On the other hand, the observed changes in the  $h_3^2$  coefficient show almost no evidence of decadal fluctuation, which is clearly seen in the predicted variation. It is possible that the nearly linear increase in the observed  $h_3^2$  is due to changes in the geodynamo. Consequently, I remove the linear trend and compare the resulting observations (circles) against the model predictions in Figure 4.5. The amplitude of the detrended fluctuation in the  $h_3^2$  is now much smaller than the predicted variation (unlike the case with  $g_3^2$ ). Therefore the phase of the conductivity pattern must be adjusted to diminish the response in the  $\tilde{h}_3^2$  coefficient and increase the response in  $\tilde{g}_3^2$  while keeping the amplitude of the conductivity variation identical to that predicted using the topography

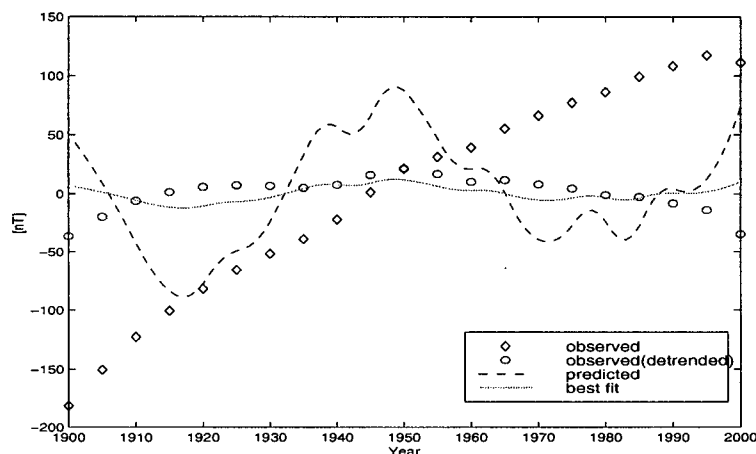


Figure 4.5: Comparison between the observed variations in  $h_3^2$  Gauss coefficients [IGRF, *Langel*, 1992] and predicted variations caused by the fluctuations in the axial dipole field.

model of *Forte et al.* [1995]. Better agreement between the predicted and observed fluctuations in the Gauss coefficients is obtained when the conductivity pattern of  $\sigma_2^2$  is rotated clockwise by an angle of  $20^\circ$ .

When the same procedure is applied to the equatorial dipole coefficients  $g_1^1$  and  $h_1^1$ , the results are inconclusive because the observed variations are substantially larger than the predicted variations (Figure 4.6). This suggests that changes in the geodynamo at  $g_1^1$  and  $h_1^1$  overwhelm any signature that arises from lateral variations in electrical conductivity. The most that can be said about the  $g_1^1$  and  $h_1^1$  coefficients is that the model predictions are not incompatible with the observed variations. Similar arguments could be made about the  $g_3^2$  and  $h_3^2$  coefficients because the observed variations may be unrelated to the effects of the lateral variations in electrical conductivity. On the other hand, the conductivity of the sediment layer could not be much larger than the values adopted here since the predicted variations would be too large to be compatible with the

observations. However, lower values of conductance cannot be ruled out if the observed variations in  $g_3^2$  and  $h_3^2$  have another source.

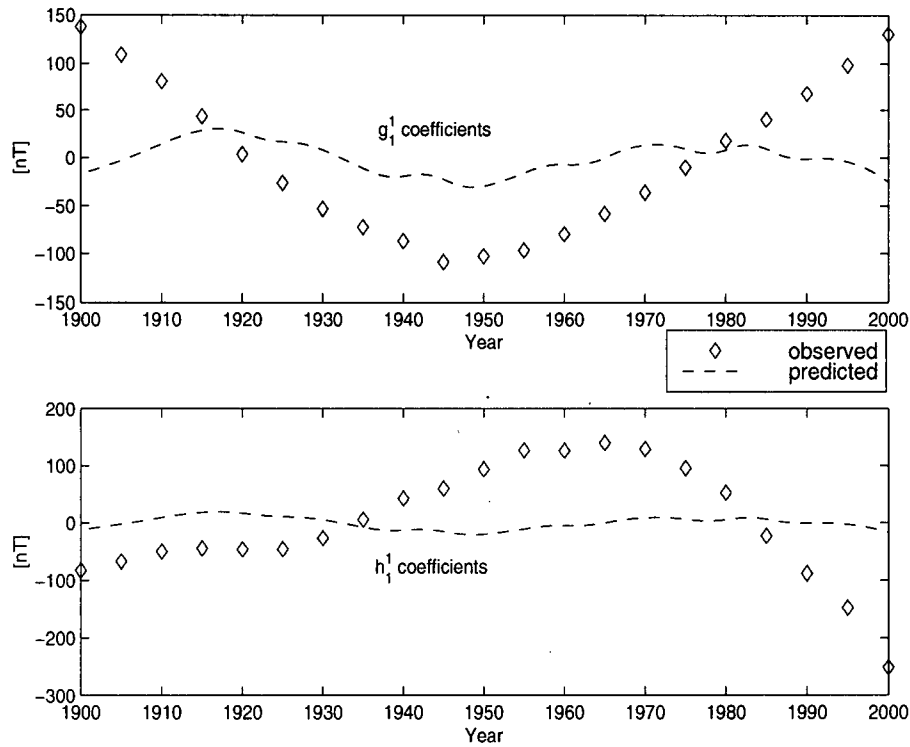


Figure 4.6: Comparison between the variations of the equatorial dipole coefficients [IGRF, Langel, 1992] and predicted variations caused by the fluctuations in the axial dipole field.

The validity of these assumptions has been tested on a data set which covers a longer period of time. The secular variation model *gufm 1* [Jackson *et al.*, 2000] provides data for the last 400 years, however, only the last half of it can be used in my analysis. This happens because absolute intensity of the magnetic field was not measured prior to 1832 and therefore the time variation of the axial dipole  $g_1^0$  cannot be computed for a period prior to 1832 (Figure 4.7).

The analysis of the data has been done in the same way as in the previous case, but



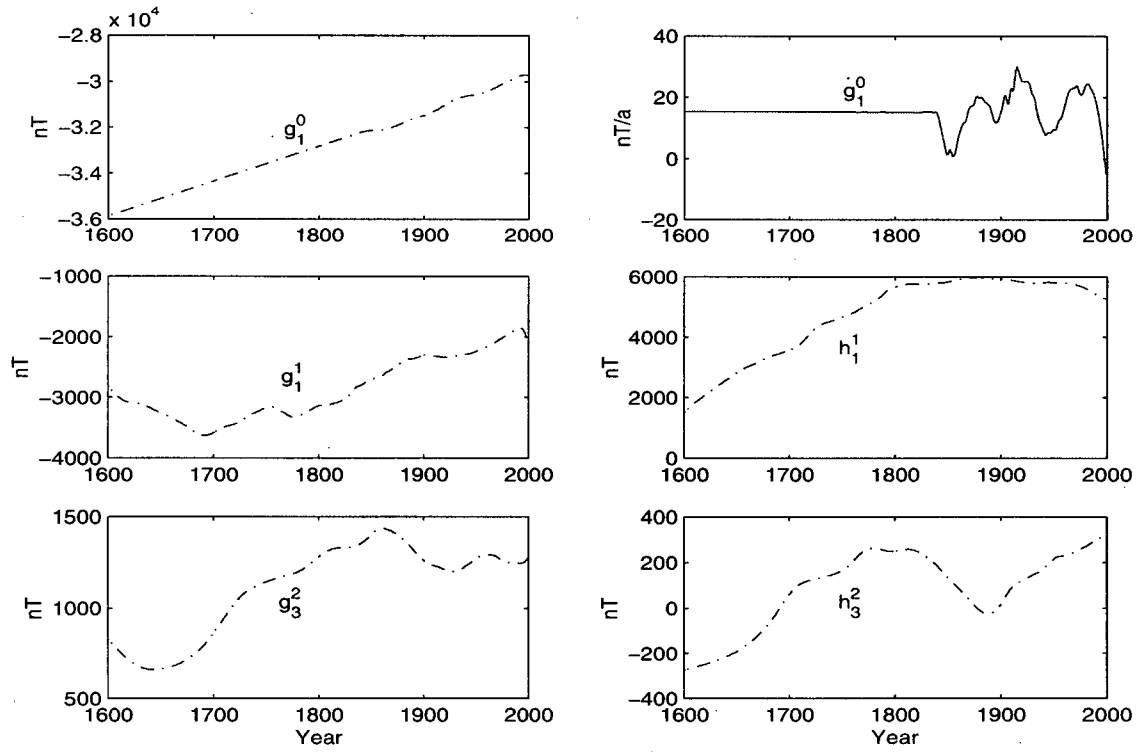


Figure 4.7: Secular variation model *gufm 1* [Jackson *et al.*, 2000] used to test the constraints on conductivity pattern.

this time I have used the time-derivative of the axial dipole provided by the *gufm 1* model [Jackson *et al.*, 2000], rather than compute it. The same steps were followed, removing the mean and linear trends when necessary. The predictions of Gauss coefficient variations were computed using the conductivity distribution of the topography-based model and subsequently of the distribution constrained by the SV data.

Inspection of the variation of the  $g_3^2$  coefficients in Figure 4.8 (top) shows that the variability observed in the IGRF model is present at earlier times. In addition, it appears that the constraints derived earlier are compatible with the longer dataset. The variation of the  $h_3^2$  coefficients (Figure 4.8 bottom) shows that the linear trend observed in the last century is part of a larger variation. Small-scale variations are buried in the much larger

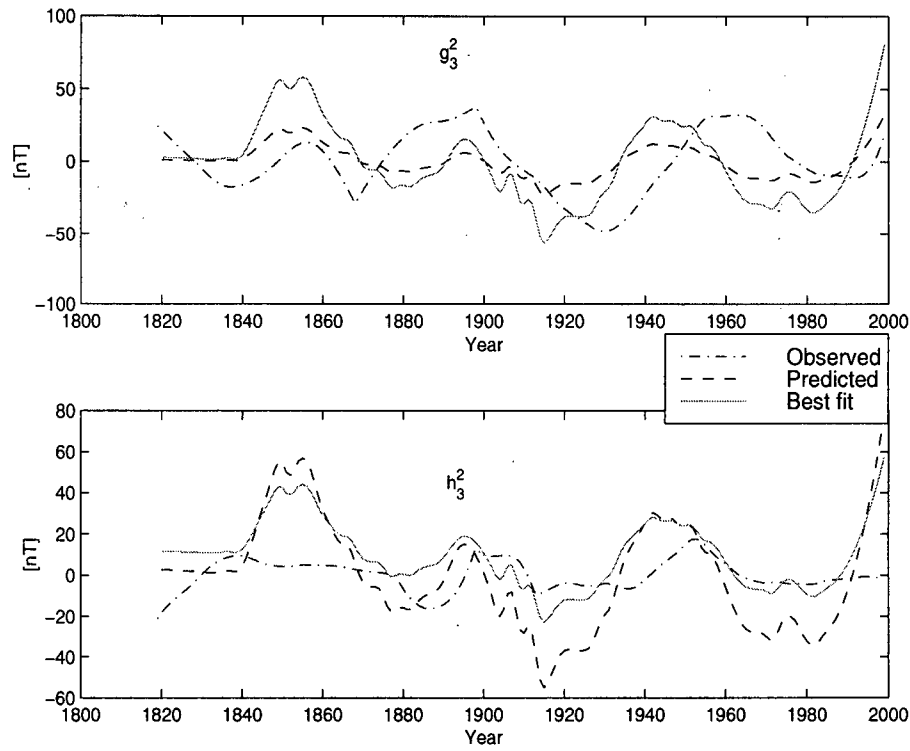


Figure 4.8: Comparison between the variations in the  $g_3^2$  and  $h_3^2$  Gauss coefficients of the *gufm 1* model [Jackson *et al.*, 2000], and predicted variations caused by the fluctuations in the axial dipole field. (Note: Linear trends have been removed from the observations.)

linear trend. As in the case of the  $g_3^2$  coefficients, the same remark can be made for the  $h_3^2$  coefficients, that the variability observed in the IGRF model is present at earlier periods. The *gufm 1* model shows that both  $Y_3^2$  coefficients, which represent an octupole effect, have a large range of variation over the last four centuries. However, following the same analysis as for the IGRF model, once the linear trends are removed and the derived constraints are applied, a reasonable fit to the data is obtained (Figure 4.8).

It is interesting to notice the apparent time delay between the observed and best-fitting models for the octupole field. The ten-year lag, present in both analyses is too

large to be attributed to differential diffusion times between the  $l = 1$  and  $l = 3$  components of the magnetic field [Smylie, 1965]. It is more likely that other processes contribute to the  $g_3^2$  and  $h_3^2$  coefficients. For example, variations in the toroidal field at the CMB, possibly linked to variations in the axial dipole, can contribute to the  $g_3^2$  and  $h_3^2$  coefficients through magnetic scattering [Koyama, 2002].

Referring now to the changes in the equatorial dipole, the high amplitude variation observed in the previous analysis is evident over the past four centuries. Predicted

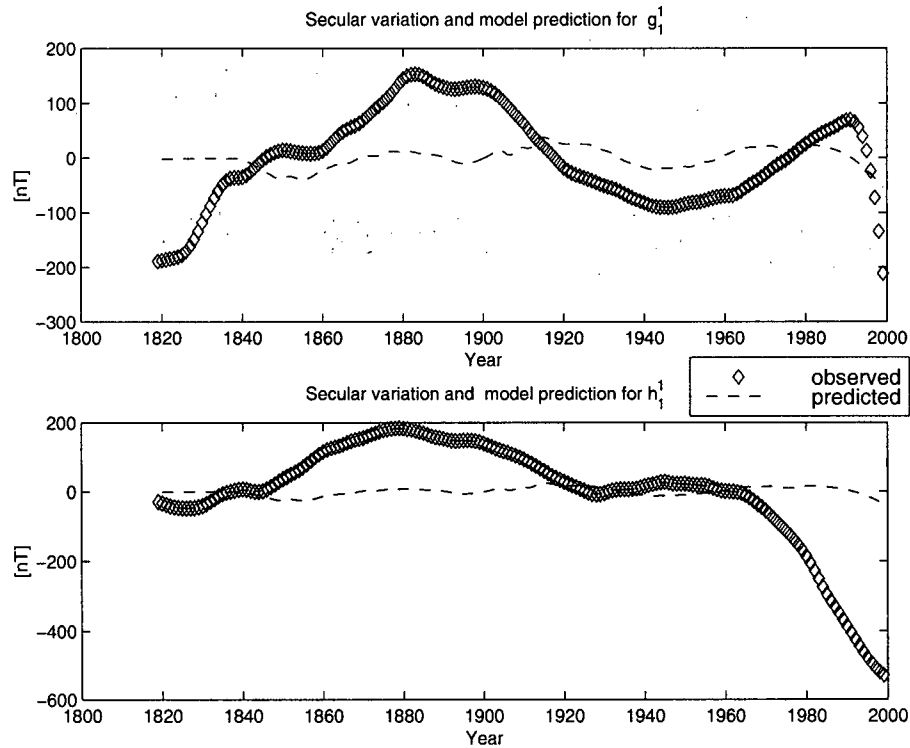


Figure 4.9: Comparison between the variations of the equatorial dipole coefficients of the *gufm 1* model [Jackson *et al.*, 2000], and predicted variations caused by the fluctuations in the dipole field.

coefficients have a much smaller variation than the historical secular variation model, which also displays rapid variations due to geomagnetic jerks [Bloxham *et al.*, 2002].

Consequently it is not possible to decipher the variations induced by the conductive layer (Figure 4.9). Increasing the amplitude of the predicted variation in the  $g_1^1$  and  $h_1^1$  coefficients would require an increase in the conductance of the layer beyond the predictions of the sediment model of *Buffett et al.* [2000]. Fine tuning was possible in the case of the octupole coefficients  $g_3^2$  and  $h_3^2$  because the applied treatment affected only the phase of the conductance, and not its amplitude, and therefore the constraints imposed by the topography and sediment models were preserved.

The attempt to fit the model predictions to the observed variability in the historical field slightly changes the phase of the conductivity model TC and consequently the configuration of the perturbation field  $\tilde{\Phi}$ . The new constraints are sought in order to improve the fit between the observed and predicted VGP paths during a reversal. To obtain a different configuration for the perturbation field, we could also assume that non-axial-dipole terms of the geodynamo field are inducing secondary field components in the layer. Observations indicate complex temporal variation in all components, however, this variation is merely a random process that cannot necessarily be linked to the decay of the axial dipole (which presumably causes the polarity reversal in the magnetic field). On the other hand, higher order components of the magnetic field would yield perturbations which are very rapidly attenuated by the presence of the mantle. For these reasons, the effect produced in the layer by temporal variation of non-dipole components of the magnetic field has not been assessed. This doesn't rule out possible strong effects of non-dipolar transition fields of core origin on reversal paths, as pointed out by a number of papers [*e.g.* *Clement*, 1991; *Bogue*, 1991; *Gubbins and Kelly*, 1993].

In the subsequent discussion I assume that the fluctuations in  $g_3^2$  and  $h_3^2$  are caused by lateral variations in electrical conductivity and adopt the best-fitting conductivity model for the  $Y_2^2$  part of  $\sigma$ . For the sake of consistency the same phase shift is adopted for the  $Y_2^1$  part of  $\sigma$ . This conductivity model is called the CC model, standing for constrained

conductivity. The resultant pattern of conductance is shown in Figure 4.10. The total conductance of the layer varies from 1 to  $1.976 \times 10^8$  S. This constrained parameter is close to the  $1.7 \times 10^8$  S value, predicted by the sediment model and is sufficient to explain the nutation observations [Buffett *et al.*, 1992]. The conductivity parameters used for both models are presented in Table 4.1, whereas Table 4.2 contains the values for the computed Gauss coefficients during a reversal. The new configuration is adopted to predict VGP paths during a reversal. Since the phase shift of the model is small (about  $20^\circ$  in longitude), the layer preserves an anomalous conductive region below the Pacific region, where the sediment model based on dynamic topography of the boundary predicts the presence of iron-enriched material.

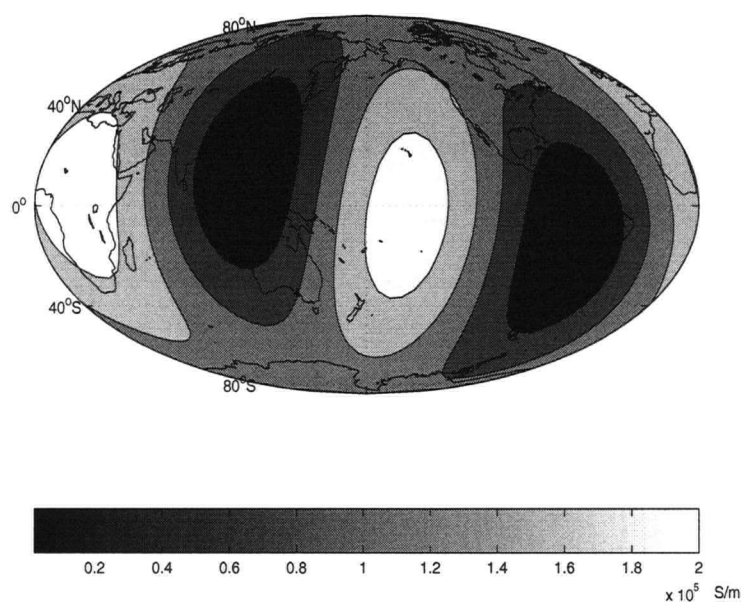


Figure 4.10: The constrained conductivity model (CC) obtained using observations of secular variation from historical magnetic field.

### 4.3 VGP Paths Obtained with a Constrained Model

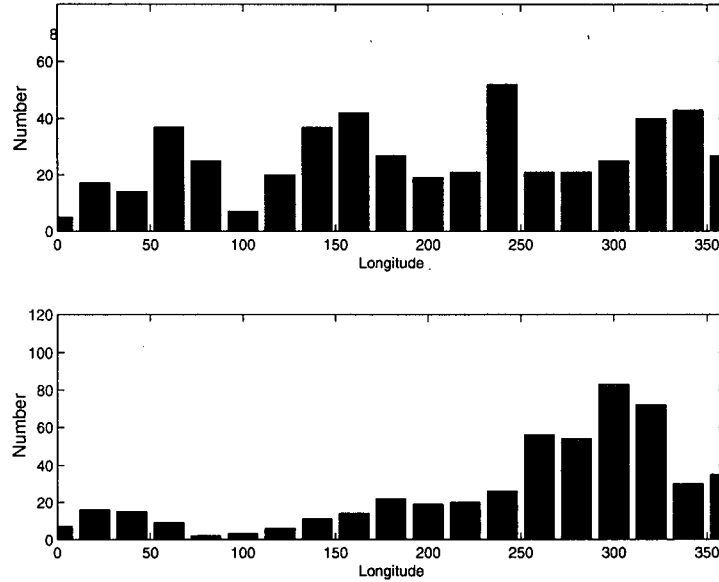


Figure 4.11: **Top:** VGP paths obtained for a field which contains the axial dipole and the  $Y_3^2$  part of the perturbation. **Bottom:** VGP paths obtained when adding the  $Y_1^1$  part of the perturbation to the above field. Perturbation given by the constrained conductivity model CC.

The effect of the constrained model CC is tested on the same 500 sites randomly distributed on the Earth's surface. The effects of the  $Y_1^1$  and  $Y_3^2$  components of  $\tilde{\Phi}$  are tracked separately as in the case of the TC model. As expected, the paths are shifted slightly in longitude by the angle of rotation of the conductivity pattern. When the effects of the  $Y_1^1$  and  $Y_3^2$  parts of  $\tilde{\Phi}$  are combined, the histograms of the VGP longitudes show a concentration of paths along American longitudes (Figure 4.11), due to the  $Y_1^1$  part in the perturbation field. The effect of the equatorial dipole (*i.e.*,  $Y_1^1$ ) term of  $\tilde{\Phi}$  is overwhelming. In one realisation of the random sites, 200 of the 500 VGP paths fall between the  $280^\circ$  and  $340^\circ$  longitudes. Apart from the preferred paths through North

America, the rest of the paths are scattered and no other geographical confinement of paths emerges. Clearly, when the conductivity pattern is constrained by the secular variation, the predicted American paths are in better agreement with the observations.

**Table 4.1. Conductivity coefficients**

Model	$\sigma_{2,2}^g$	$\sigma_{2,2}^h$	$\sigma_{2,1}^g$	$\sigma_{2,1}^h$	Total RMS [S/m]
TC	$55.86 \times 10^3$	$137.92 \times 10^3$	$-40.65 \times 10^3$	$26.91 \times 10^3$	$19.76 \times 10^4$
CC	$128.53 \times 10^3$	$75.0 \times 10^3$	$-29.79 \times 10^3$	$38.59 \times 10^3$	$19.76 \times 10^4$

**Table 4.2. Gauss coefficients of the perturbation  $\tilde{\Phi}$** 

Model	$g_3^2$	$h_3^2$	$g_1^1$	$h_1^1$	Total RMS [nT]
TC	92.91	-229.39	-156.04	103.25	434.61
CC	-213.76	-124.73	-114.33	148.11	434.61



## Chapter 5

### ADDITIONAL RESULTS

#### 5.1 Tests on the Paleomagnetic Database

The analysis of synthetic data from 500 randomly distributed sites represents an ideal situation for the study of the paleomagnetic field, because the pseudo-record contains a large number of sites evenly spread over the Earth's surface. In reality, observations come from a smaller number of rocks unevenly sampled around the globe. Consequently, it is of interest to ask how the conclusions of the previous chapter change if the analysis is restricted to sites in existing databases. As a first test, I take a distribution of sites from the volcanic database [Love, 1998], which contains 63 magnetic measurements of lavas sampled in Iceland, Greece, British Columbia, Hawaii and Africa. I run the reversal simulation and use the perturbation field given by the CC model.

This non-uniform sampling yields a different distribution of paths from the one obtained from the uniform spreading of sites (Figure 5.1). The distribution shows preferred paths along the Asian and American longitudes as well as mid-Pacific. Two of the paths are in agreement with the paths found by Love in analyzing the data. I also examine the paths for prominent sites in the database. The predicted paths for several sites in Iceland are confined to longitudes through Asia, which is in agreement with the observations. In fact, the large number of Icelandic observations in the volcanic database shifts the preferred paths in Figure 5.1 to longitudes through Asia. In contrast, the preferred paths inferred from a more uniform distribution of sites were confined only to longitudes

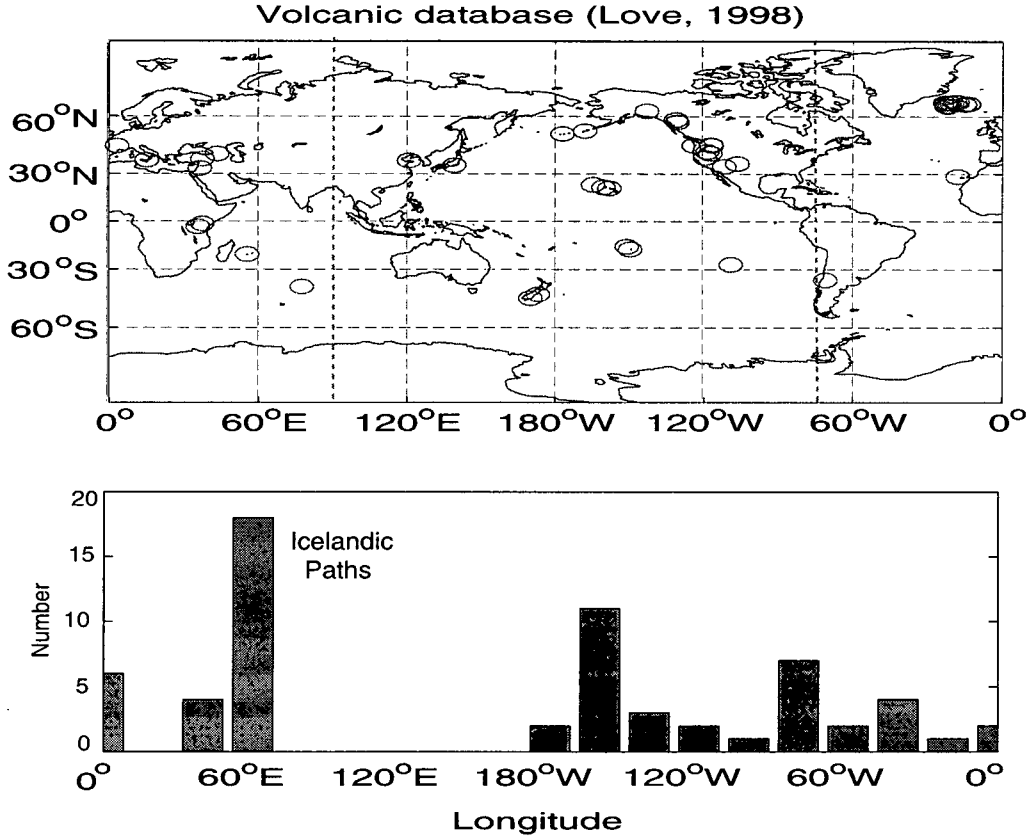


Figure 5.1: VGP paths for a distribution of sites in volcanic database (*Love, 1998*). The dashed lines on the upper panel indicate the preferred paths obtained from the volcanic database. The lower panel gives the predictions of the model when the same sites are used.

through North America.

The effect of the perturbation field was also tested on a data set containing magnetic measurements of lake and oceanic sediments. For this, I use a compiled database consisting of 21 records of the same reversal, mostly sampled from Atlantic and Pacific ODP locations [*Clement, 1991*]. (*Clement's* study has also implied the presence of preferred VGP paths through the Americas and Asia.) The histogram showing the distribution of the VGP paths obtained with my model reveals geographical confinement of paths

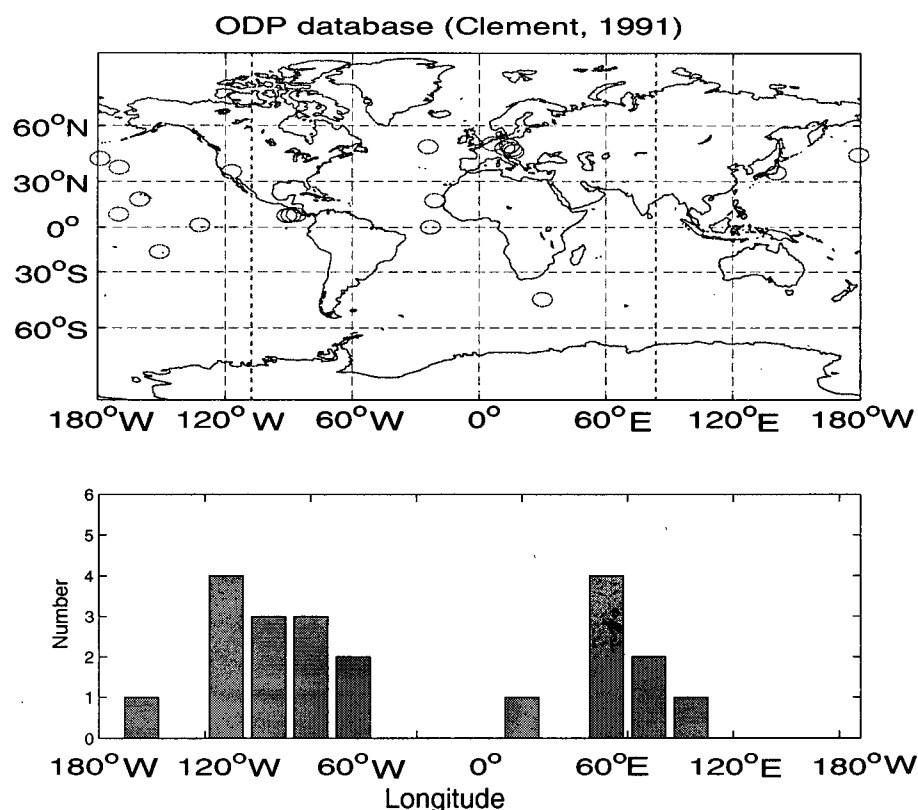


Figure 5.2: VGP paths for a distribution of sites in oceanic sediments database (Clement, 1991). The dashed lines on the upper panel indicate the paths obtained from the sediment database. The lower panel gives the predictions of the model when the same sites are used.

through North America and Asia. (Figure 5.2). The American paths cover a wide sector of longitude, peaking at approximately 100° W, in good agreement with the observations.

Finally, I consider a data set compiled by *Gubbins and Coe* [1993], which include both volcanic and sedimentary data. To this dataset I add several sites (Iceland, Greece) to define a representative collection of sites. The locations have provided paleomagnetic measurements on lavas (*e.g.*, Hawaii, Iceland, British Columbia) and deep-sea sediments (*e.g.*, Atlantic, Greece, Pacific). My model yields reversal paths which are with one

exception confined to longitudes which cover Asia and North America (Figure 5.3). The plot shows a geographical confinement around the Pacific rim, as was very often suggested by the observations. The bi-modal distribution of paths has prompted various suggestions for the mechanism that generates the preferred VGP paths, most of them based on the apparent symmetry of the preferred paths. The Asian paths in my model occur due to sampling of European sites. As it is possible that records coming from this part of the world have been extensively used for paleomagnetic measurements, I speculate that the preferred Asian paths might be an artifact of uneven sampling.

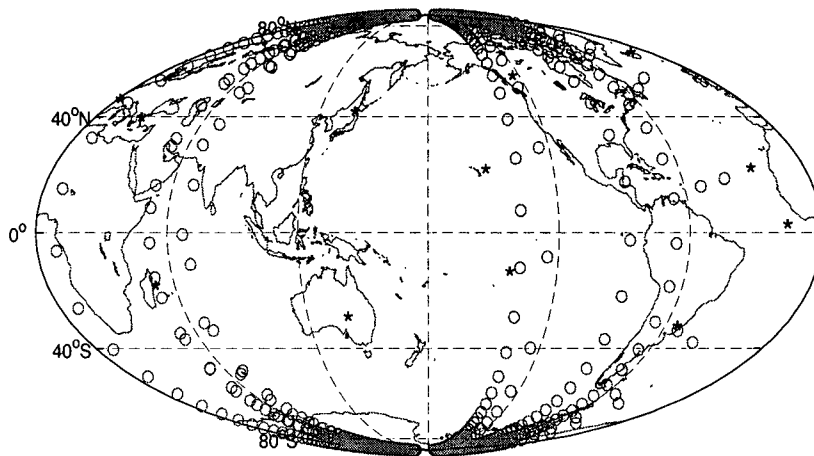


Figure 5.3: VGP paths for twelve sites compiled from the palaeomagnetic database.

It is clear from these examples that sampling can significantly influence the interpretation of transition fields. My results are in agreement with the observations because North American and Asian paths emerge when site locations are chosen to mimic the paleomagnetic databases. The VGP paths in my model are dependent on the sampling location because the perturbation  $\tilde{\Phi}$  contains non-axial-dipole terms, which are superimposed on the time-varying axial dipole. As seen earlier in this study, the spectrum

of the perturbation field  $\tilde{\Phi}$  depends on the structure of reversing magnetic field and the geometry of the conducting layer.

It is equally interesting to see if the perturbation is large enough to be detectable when we allow for variability of the main magnetic field. To test this, the perturbation  $\tilde{\Phi}$  is superimposed on a transition field which includes both dipole and non-dipole components. The non-axial-dipole part of the transition field is represented as a realisation of a Gaussian process, based on the geomagnetic secular variation model of *Constable and Parker* [1988]. This part of the field, which was not present in my previous analyses, is referred to as the 'background' field. The presence of the background field accounts for the natural variability of the geomagnetic field. In the next sections I describe the implementation of the statistical model and the results obtained when the background field is incorporated in the transition field.

## 5.2 Brief Description of the Transition Field Model

The secular variation of the magnetic field encompasses changes on time scales from 10 to  $10^4$  years, reflecting variations in the mechanism producing the magnetic field. Reversals of the field polarity represent a particular feature of the secular variation and, as mentioned earlier, have a duration of several thousands of years. To determine the influence of the perturbation field over the geodynamo field during a reversal, I seek to model a polarity reversal in which the main dipole field remains axial but decreases in strength during a transition so that the non-dipole part of the main field becomes significant in determining the orientation of the VGP. The question that is asked is whether the perturbation  $\tilde{\Phi}$  is large enough to leave its signature on the field in the intermediate stages of a reversal.

The temporal variability of the axial dipole term is modelled as in the previous section,

by allowing a decrease in intensity of the  $g_1^0$  Gauss coefficient followed by an increase in intensity in the opposite field direction in a time interval equal to the duration of the reversal. For the rest of the coefficients I make use of a statistical description of the field, which is an effective way to describe the characteristics of the variability in the geomagnetic field, and simpler than attempting to physically model the field at each instant.

The statistical model proposed by *Constable and Parker* [1988] separates the behaviour of the dipole and non-dipole parts in the Earth's magnetic field. It is assumed that the dipole part of the field is statistically independent from the non-dipole part. The spherical harmonic coefficients of the non-dipole field are regarded as realisations of a Gaussian distribution. At a fixed radial distance  $r$ , the quantity

$$R_l = \left(\frac{a}{r}\right)^{2(l+2)} (l+1) \sum_{m=0}^l [(g_l^m)^2 + (h_l^m)^2], \quad (5.1)$$

known as the *Mauersberger-Lowes* spectrum [*Constable and Parker*, 1988], defines the power in the magnetic field associated with each degree  $l$ . The geomagnetic field spectrum decays rapidly with increasing  $l$ . The usual interpretation of the spectrum is that the field described by terms with degree  $1 \leq l \leq 12$  originates in the core, whereas the field described by terms with  $l \geq 16$  has a crustal origin. At  $r \sim c$  the spectrum  $R_l$  is not very dependent on  $l$ , therefore indicating a 'white noise' source at the CMB.

Observations have shown that the power in  $R_l$  is evenly distributed across the angular orders  $m$  and variable in time. Therefore, the squared amplitude  $(g_l^m)^2 + (h_l^m)^2$  is also treated as a random variable. The model proposed by *Constable and Parker* (CP88) treats every spherical harmonic coefficient as a normally distributed, independent random variable and uses the Lowes spectrum as a guide in constructing the statistical model. For the non-dipole terms, the model spectrum is devised to be exactly flat at the surface

of the core. The expectation of the spectrum for the non-dipole terms of the field is

$$E[R_l] = E \left[ \sum_{m=0}^l (l+1) [(g_l^m)^2 + (h_l^m)^2] \right] = \left( \frac{c}{a} \right)^2 l \alpha^2, \quad (5.2)$$

where  $\alpha$  is a fitted parameter. The coefficients with  $l \neq 1$  are independent samples of a single zero-mean Gaussian process with variance  $(\sigma_l)^2$ , where

$$(\sigma_l)^2 = \frac{1}{(l+1)(2l+1)} \left( \frac{c}{a} \right)^2 l \alpha^2. \quad (5.3)$$

In the CP88 model, the axial dipole is treated differently since a Gaussian distribution for this term is incompatible with the observations. On the other hand, the equatorial dipole can be well fit by the Gaussian process. The terms  $g_1^1$  and  $h_1^1$  in my transition field model have been incorporated using the same statistical description as the non-dipole terms.

I have used the statistical model CP88 to generate a number of realisations of the Gaussian process, which were employed to describe different realisations of the non-axial-dipole background field. The spectrum of the coefficients is plotted in Figure 5.4. The value for the fitted parameter  $\alpha$ , which gives the variance of the distribution, has been taken from the study by *Constable and Johnson* [1999], correcting the value given in the CP88 model. The field thus constructed simulates the geomagnetic field at the Earth's surface (up to degree and order 8). The transition field is described by the fluctuations of the dipole which decreases in intensity to zero and increases in the opposite field direction. The intensity of the axial dipole term ( $g_1^0$ ) before the onset of the reversal is given by the present value of the Gauss coefficient of the geomagnetic field. The intensities of the equatorial dipole terms ( $g_1^1, h_1^1$ ) right before the reversal are given by the statistical model. The non-dipole part of the field is given by the CP88 model and is considered stationary over the period of the reversal. This is consistent with field orientation observations which suggest that significant changes in the non-dipole field have a time constant of

order 100 - 200 kyr [Elmaleh *et al.*, 2003], much longer than the duration of one reversal. Therefore my model for a transition field makes a clear distinction between the dipole terms and the non-dipole terms of the geomagnetic field. The dipole terms are allowed to vary in time, while the non-dipole terms are constant during a reversal. The perturbation  $\tilde{\Phi}$  is superimposed on the transition field.

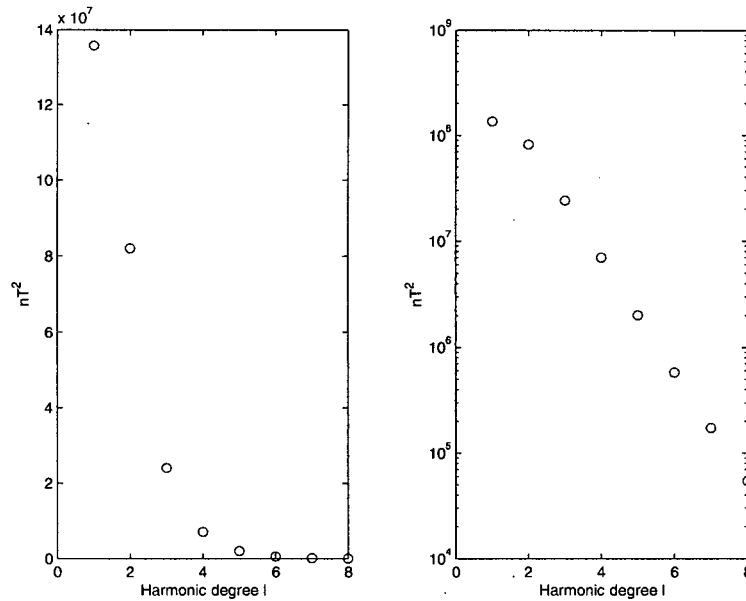


Figure 5.4: The geomagnetic field spectrum (normal and semi-log scale) at the Earth's surface, for  $l = 1$  to 8, excluding the  $g_1^0$  term. The spectrum refers to the coefficients computed using the CP88 field model.

### 5.3 VGP Paths Obtained When a Background Non-Dipole Field Is Included

The VGP paths that arise from the above field are computed for the 500 randomly distributed sites previously considered. At the beginning of the reversal process, the dipole components are close to their initial values and the longitude of the VGP paths is not affected by the presence of the perturbation field. This is because the amplitude of



the perturbation is less than 10% of the field intensity before the reversal starts. When the dipole terms have almost vanished, the orientation of the field is given by the non-dipole field and the effect of the perturbation  $\tilde{\Phi}$  becomes more significant because  $\tilde{\Phi}$  has the same order of magnitude as the non-dipole terms. My model computes the VGP paths at the moment when the dipole vanishes.

The results of a reversal with one non-dipole realisation of the magnetic field are shown in Figure 5.5. The histograms of the VGP longitudes are plotted for the transition field with and without the perturbation due to  $\tilde{\Phi}$ . The plots clearly show that the distribution

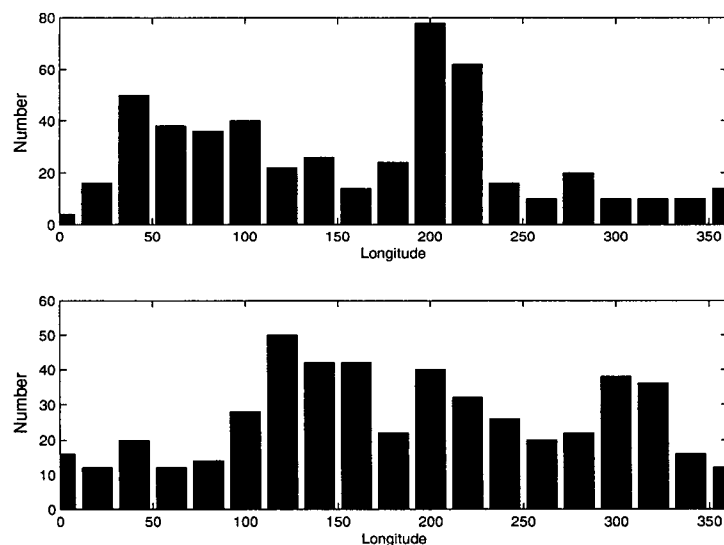


Figure 5.5: **Top:** VGP paths obtained without the magnetic perturbation. For the non-dipole terms, a realisation of the statistical model CP88 is used. **Bottom:** VGP paths obtained when the magnetic perturbation is included.

of paths is affected by the presence of  $\tilde{\Phi}$ . Inasmuch as the statistical field does not yield paths on American longitudes, the perturbation is affecting the distribution of paths,

and moves the paths to the Americas. It is noticeable from the plots that there is also a preferred path through Asia, given entirely by this one realisation of the statistical model.

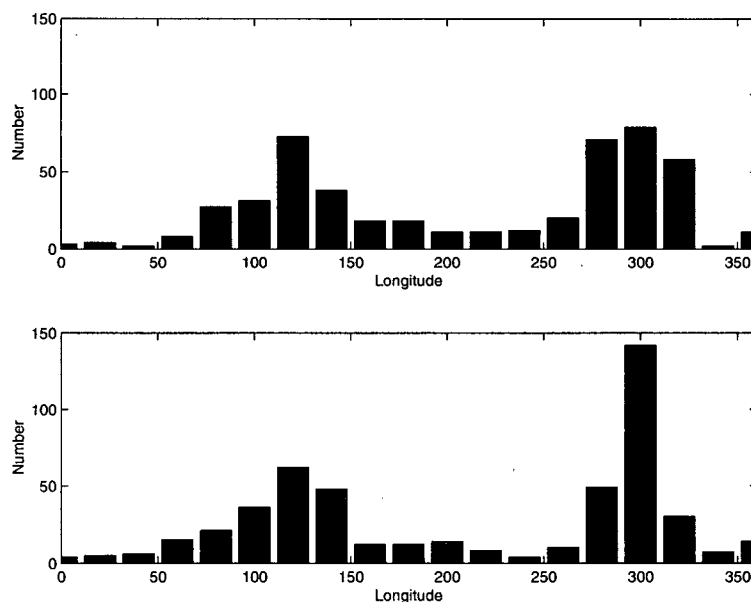


Figure 5.6: **Top:** VGP paths obtained from a statistical field. **Bottom:** VGP paths obtained when the perturbation  $\tilde{\Phi}$  is added to the above field.

Figure 5.6 shows the outcome of the experiment on another statistical realisation. This unusual example was chosen because this particular realisation of the field already gives the appearance of the two preferred paths. Superimposing the effect of the perturbation  $\tilde{\Phi}$  displaces paths from the Asian longitudes and enhances the American path. The effect of the perturbation has been tested for more realisations of the statistical model, which can be viewed as individual reversals. For all cases the results have shown that the paths are confined to American longitudes.

This experiment was concluded by averaging the results of 20 realisations of the

statistical field on 40 sites randomly distributed over the Earth's surface. As expected, when the field is unperturbed, the distribution of the VGP longitudes is nearly flat as a result of averaging a number of realisations of the statistical field model. When the perturbation is added to the field, the only outstanding feature in the distribution of the VGP paths is the concentration of paths through the American longitudes. These experiments show that the secondary magnetic field is strong enough to influence the transition field during a reversal when the dipole is decreasing in intensity. The VGP longitudes are mostly controlled by the  $Y_1^1$  geometry of the secondary field. Consequently, my results indicate that when the perturbation caused by the conductive basal layer is superimposed on a transition field, it is almost certain that preferred reversal paths through the Americas will be recorded.

The final question I consider is how the duration of the reversal affects the distribution of the VGP paths. In my model, the period of time in which the field completes a polarity reversal determines the rate of change in the dipole field. It is therefore possible that for a lower rate of change in the dipole, the secondary field will not stand out from the background field.

As an example, I take a representative site in the paleomagnetic database (Iceland) and run several reversal simulations for different durations of the reversal. I consider first that the reversal is happening in one thousand years and then the duration of reversal is increased to four thousand years. For each case I average the VGP paths over 20 and later 40 reversals. The results of this experiment show that the distribution of the VGP longitudes during a reversal is sensitive to the time interval in which a reversal is happening (Figure 5.7). For a slower reversal, the amplitude of  $\tilde{\Phi}$  is not high enough to yield preferred VGP paths. The preferred path through Asia is obvious for a faster reversal, whereas for a slower reversal the distribution of VGP paths is more uniform. I conclude that preferred VGP paths are more likely to be recorded when the reversal is

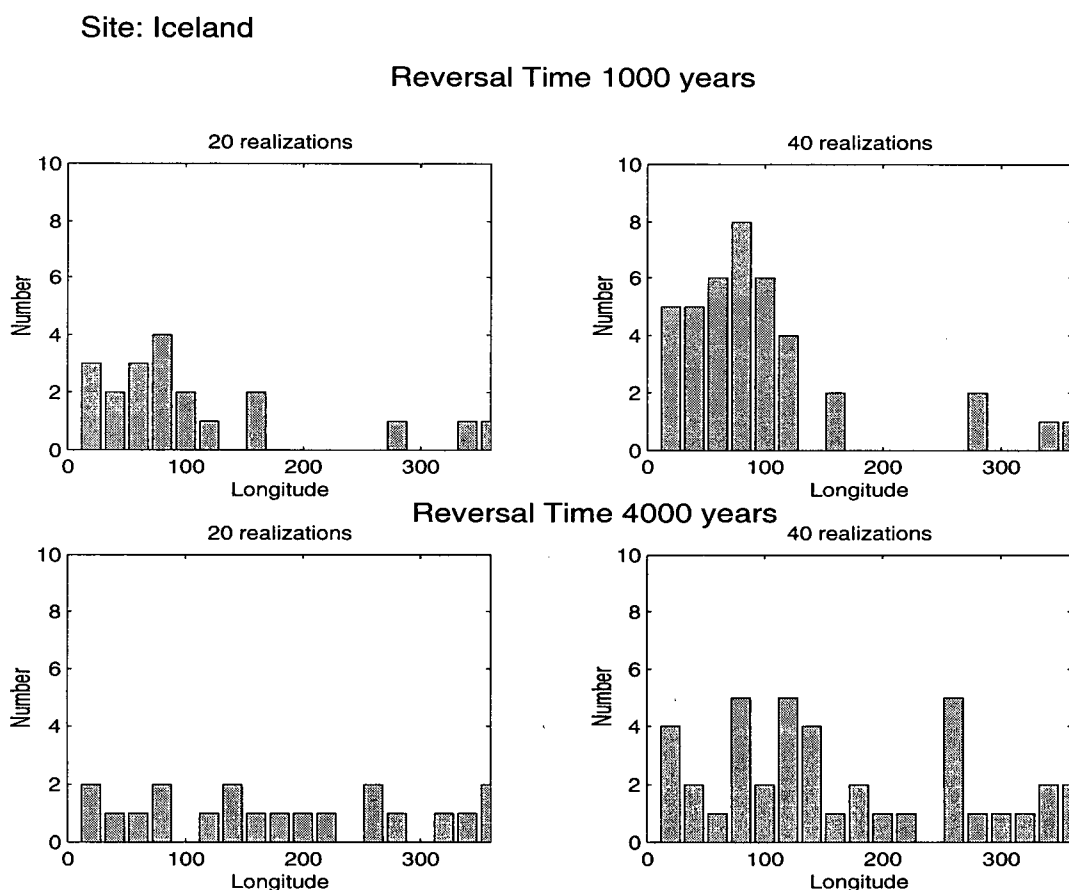


Figure 5.7: VGP paths obtained for different durations of polarity reversals.

rapid (*i.e.*, 1000 - 2000 years). In order for slower reversal to produce preferred paths, my model requires an initial dipole intensity higher than the present-day value, so that the rate of change in  $g_1^0$  is sufficiently large.

The same experiment shows that the probability of recording preferred VGP paths increases with the number of reversals. Figure (5.7) displays the histograms of VGP paths recorded in the same location for 20 and 40 reversals. For a faster reversal, the preferred paths through Asia are more evident when the number of reversals increases. For the slower reversal case, the distribution of paths is quite flat when only 20 reversals

are taken into account. However, increasing the number of reversals tends to emphasize the paths through Asia.

## Chapter 6

### DISCUSSION AND CONCLUSIONS

The goal of this thesis was to study the effect of a highly conducting layer at the base of the mantle on the magnetic field during a polarity reversal. The existence of preferred VGP paths during a reversal has received much interest among the paleomagnetic community and the model proposed in the present study provides a plausible explanation for this phenomenon. My study has been equally interesting, challenging and rewarding and presents opportunities for further research. The main findings of the thesis are summarized below.

#### Preferred Reversal Paths

The model developed in this work has shown that induction of a secondary magnetic field in a highly conductive layer at the base of the mantle can alter the non-axial dipole part of the Earth's magnetic field and hence produce preferred reversal paths. The secondary field is generated by electric currents in the conducting layer, which are induced by temporal variations in the dipole part of the magnetic main field. The perturbation is characterized at the Earth's surface by equatorial dipole ( $Y_1^1$ ) and non-dipolar ( $Y_3^2$ ) terms. When the polarity reversal occurs through a decrease in the dipole field, in the absence of the perturbation, the positions of the VGP are determined by the non-dipole components of the field. The non-dipole part of the Earth's magnetic field is believed to be mainly isotropic [Constable and Parker, 1988; Constable and Johnson, 1999; Quidelleur and Courtillot, 1996] and my study treats the  $g_l^m$  and  $h_l^m$  Gauss coefficients with  $l \geq 2$  as

zero-mean, normally distributed, independent variables. The VGP paths obtained for an unperturbed transition field were randomly distributed in longitude, with no persistent geographical confinement from one reversal to another.

The addition of the secondary field to the non-dipole field systematically affects the transition field at the surface. The largest effect is due to the  $Y_1^1$  component of the perturbation. Superposition of the perturbation field over the pre-existent non-dipole field makes the geomagnetic field anisotropic during a reversal which yields preferred locations of the magnetic pole. A perturbation generated by temporal variations of the dipole in a variably conducting layer with a configuration close to the CMB topography yields preferred reversal paths through the American longitudes.

### **One or more preferred paths?**

The research presented in this thesis provides a physical explanation for producing preferred VGP paths during a reversal. The results show that the reversal paths given by a uniform distribution of sites have an asymmetric pattern, revealing a strong concentration of paths on the American longitudes. When using a non-uniform sampling of sites (reproducing the uneven distribution of real data), the model yields Asian and American paths. These distributions of paths are in agreement with the observations, which generally find two preferred paths, one of them following American longitudes. The bi-modal distribution of paths through the Americas and Asia was documented in the Matuyama-Brunhes transition [*e.g.*, *Laj et al.*, 1991], whereas grouping of reversal paths through the Americas only was observed in the Upper Olduvai reversal [*e.g.*, *Tric et al.*, 1991]. My results showing longitudinal confinement of paths are consistent with the observations, but also show that non-uniform sampling can influence the interpretation of the reversal paths distribution.

### Persistence of equatorial dipole terms during a reversal

Previous works have shown that the equatorial dipole part of the present field (or of a paleo-field with a similar configuration) has an important influence on the reversal paths during a reversal [Constable, 1992; Gubbins and Sarson, 1994]. My tests have revealed that for a reversal in which the equatorial dipole persists through a reversal, the additional field caused by the conducting layer is too small to affect the distribution of the reversal paths.

However, a transition field characterized by decreases in both the axial and equatorial dipoles, is significantly affected by the magnetic perturbation, causing a geographical confinement of VGP paths to American longitudes. The clustering of paths over the Americas in my model is due to the  $Y_1^1$  component of the secondary field produced in the conductive layer by decreases in the axial dipole. This term of the perturbation has the same geometry as the equatorial dipole. Additional computations have shown that temporal variations in the equatorial dipole (say during a reversal) also induce perturbations with  $Y_1^1$  terms, although of smaller amplitude than those caused by decreases in the axial dipole. A persistent perturbation with  $Y_1^1$  dependence suggests that an equatorial dipole could be present in the geomagnetic field at the surface, even if the axial and equatorial dipoles of the geodynamo normally vanish during the reversal. The persistence of equatorial dipole terms in the field is important because these long wavelength terms strongly influence the field direction, thereby producing preferred reversal paths.

### Duration of the reversal and the strength of the dipole

Computations show that the magnetic field generated by variations in the axial dipole  $g_1^0$  has the largest influence on the VGP paths. The amplitude of the perturbation field in my model depends on the initial value of the axial dipole intensity and the duration of



the reversal, which define the rate of change in the magnetic field. Temporal variations in the non-axial-dipole components produce much smaller perturbations due to the smaller rate of change.

The results in the previous chapter show that the VGP preferred paths are more likely to occur when the magnetic field reverses itself in about 2000 years or so. For this situation, the rate of change in the axial dipole is sufficient to cause a perturbation that rises above the natural variability in the non-dipole, background field. As an example, preferred Asian paths were detectable for sampling sites located in Iceland for a reversal that occurred in 1000 years. On the other hand, the tests have shown that for slower reversals, the rate of change in the axial dipole decreases to the point where the perturbation has a weak influence on the VGP paths. For Icelandic sites, some preferred VGP paths were detectable only if a larger number of reversals were averaged. Real data sets do not usually provide a large number of reversals for the same site. Based on my model, we can conclude that for slower reversals, which generate weaker perturbations, the chance of recording preferred paths is smaller. The model can however yield preferred VGP paths for slower reversals if the dipole field at the onset of reversal is stronger than the present-day value.

### **Conductivity at the base of the mantle**

The occurrence of preferred VGP paths in my model is due to the magnetic perturbation generated within the thin, conducting layer in the lowermost mantle. Lateral variations in conductivity at the core-mantle interface are given by the compositional heterogeneity as a result of secular cooling of the core [Buffett *et al.*, 2000]. The conductivity model devised for the study of VGP paths is constrained by the predictions of the sediment accumulation model and the dynamic model of CMB topography [Forte *et al.*, 1995].

Additional constraints on the conductivity structure are sought in order to improve the fit between predictions and observations of VGP reversal paths. For this, I use the variability in the secular variation (SV) data to detect the signature of the conductive layer in modern observations. The analysis of SV data supports the interpretation that fluctuations in the non-dipole field can be attributed to the effect of fluctuations in the axial dipole in a conductive layer at CMB. However, the model constrains the conductance of the layer to be no more than  $1.9 \times 10^8$  S in order to fit the amplitude of the secular variation observations. This upper bound for the conductance is in agreement with the predictions of the sediment model [Buffett *et al*, 2000] and is sufficient to explain the nutation observations [Buffett, 1992].

### **Configuration of the CMB and time constraints on lower mantle dynamics**

The influence of the conductive layer on the VGP paths can persist for several hundred million years before the conductivity pattern changes at the base of the mantle. The time scale for altering the conducting layer is probably related to the time scale for changing topography at the CMB. Thereby changes in the distribution of the conducting material would take place on a time scale of  $10^8$  years. In this case, the geometry of the preferred paths can be the same for several reversals but we might find gradual changes in the preferred paths over time scales longer than  $10^8$  years. The length of the period for which the same pattern for reversal paths is maintained can provide time constraints on the lower mantle convection and hence contribute to the understanding of the core-mantle interactions. However, this hypothesis might prove difficult to test with the relatively reduced number of observations we have today.

## References

- Aurnou, J.M., Buttles, J.L., Neumann, G.A., Olson, P.L., Electromagnetic core-mantle coupling and paleomagnetic reversal paths, *Geophys. Res. Lett.*, 23, 2,705-2,798, 1996.
- Bloxham, J., Zatman, S., Dumberry, M., The origin of the geomagnetic jerks, *Nature*, 420, 65-68, 2002.
- Bogue, S., Reversals of opinion, *Nature*, 351, 445-446, 1991.
- Brito, D., Aurnou, J.M., Olson, P.L., Can heterogeneous core-mantle electromagnetic coupling control geomagnetic reversals?, *Phys. Earth Planet. Int.*, 112, 159-170, 1999.
- Buffett, B.A., Constraints on magnetic energy and mantle conductivity from forced nutations of the Earth, *J. Geophys. Res.*, 97, 19,681-19,597, 1992.
- Buffett, B.A., Garnero, E.J., Jeanloz, R., Sediments at the top of the Earth's core, *Science*, 290, 1,338-1,342 2000.
- Cande, S.C., Kent, D.V., Revised calibration of the geomagnetic polarity timescale for the late Cretaceous and Cenozoic, *J. Geophys. Res.*, 100, 6,093-6,095, 1995.
- Clement, B.M., Geographical distribution of transitional VGPs: evidence for non-zonal equatorial symmetry during the Matuyama-Brunhes geomagnetic reversal, *Earth Planet. Sci. Lett.*, 104, 48-58, 1991.
- Constable, C.G., Link between geomagnetic reversal paths and secular variation of the field over the past 5 Myr, *Nature*, 358, 230-233, 1992.

- Constable, C.G., Johnson, C.L., Anisotropic paleosecular variation models: implications for geomagnetic field observables, *Phys. Earth Planet. Int.*, 115, 35-51, 1999.
- Constable, C.G., Parker, R.L., Statistics of the geomagnetic secular variation for the past 5 m.y., *J. Geophys. Res.*, 93, 11,569-11,581, 1988.
- Cox, A., Doell, R.R., Dalrymple G.R., Reversals of the Earth's magnetic field, *Science*, 144, 1537, 1964.
- Creer, K.M., Ispir, Y., An interpretation of the behaviour of the geomagnetic field during polarity transitions, *Phys. Earth Planet. Int.*, 2, 283, 1970.
- Elmaleh, A., Valet, J.-P., Quidelleur, X., Solihin, A., Bouquerel, H., Tesson T., Mulyiadi, E., Paleosecular variation in Java and Bawean Islands (Indonesia) during the Brunhes chron, *Geophys. J. Int.*, In Press.
- Forte, A.M., Mitrovica, J.X., Woodward, R.L., Seismic-geodynamic determination of the origin of excess ellipticity of the core-mantle boundary, *Geophys. Res. Lett.*, 22, 1013-1016, 1995.
- Fuller, M., Williams, I., Hoffman, K.A., Palaeomagnetic records of geomagnetic field reversals and the morphology of the transitional fields, *Rev. Geophys. Space Phys.*, 17, 179, 1979.
- Garnero, E.J., Heterogeneity of the lowermost mantle, *Ann. Rev. Earth Planet. Sci.*, 28, 509-537, 2000.
- Garnero, E.J., Jeanloz, R., Fuzzy patches on the core-mantle boundary, *Geophys. Res. Lett.*, 27, 2777-2780, 2000.
- Garnero, E.J., Revenaugh, J., Williams, Q., Lay, T., Kellog, L. H., Ultra-low velocity zones at the core-mantle boundary, *The Core-Mantle Boundary*, M. Gurnis, M.E. Wyssession, E. Knittle, B.A. Buffett editors, 319-334, 1998.

- Garnero, E.J., Helmberger, D.V., A very slow basal layer underlying large-scale low-velocity anomalies in the lower mantle beneath the Pacific: evidence from core phases, *Phys. Earth Planet. Int.*, 91, 161-176, 1995.
- Garnero, E.J., Helmberger, D.V., Seismic detection of a laterally varying boundary layer at the base of the mantle beneath the central-Pacific, *Geophys. Res. Lett.*, 23, 977-980, 1996.
- Glatzmaier, G.A., Roberts, P.H., A three-dimensional self-consistent computer simulation of a geomagnetic field reversal, *Nature*, 377, 203-209, 1995.
- Gubbins, D., Geomagnetic polarity reversals - a connection with secular variation and core-mantle interaction, *Reviews of Geophysics*, 32, 61-83, 1994.
- Gubbins, D., Coe, R.S., Longitudinally confined geomagnetic reversal paths from non-dipolar transition fields, *Nature*, 362, 51-53, 1993.
- Gubbins, D., Kelly, P., Persistent patterns in geomagnetic fields over the past 2.5 Myr., *Nature*, 365, 829-832, 1993.
- Gubbins, D., Roberts, P.H., Magnetohydrodynamics of the Earth's Core, *Geomagnetism*, Vol. 2, J.A. Jacobs editor, Academic Press, London, UK, 1-184, 1987.
- Gubbins, D., Sarson, G., Geomagnetic field morphologies from a kinematic dynamo model, *Nature*, 368, 51-55, 1994.
- Gubbins, D., Love J.J., VGP paths during geomagnetic polarity reversals: Symmetry considerations, *Geophys. Res. Lett.*, 25, 1,079-1,082, 1998.
- Hammond, S.R., Seyb, S.M., Theyer, F., Geomagnetic polarity transitions in two oriented sediment cores from the northwest pacific, *Earth Planet. Sci. Lett.*, 44, 167, 1979.

- Herrero-Bervera, E., Runcorn, S.K., Transition fields during geomagnetic reversals and their geodynamic significance *Phil. Trans. R. Soc. London, A*, 355, 1,713-1,742, 1997.
- Herrero-Bervera, E., Theyer, F., Helsey, C.E., Olduvai onset polarity transition: two detailed paleomagnetic records from North Central Pacific sediments *Phys. Earth Planet. Int.*, 49, 325-342, 1987.
- Hoffman, K.A., Dipolar reversal states of the geomagnetic field and core-mantle dynamics, *Nature*, 359, 789-794, 1992.
- Hoffman K.A., Fuller, M., Transitional field configuration and geomagnetic reversal, *Nature*, 273, 715, 1978.
- Holme, R., Electromagnetic core-mantle coupling III. Laterally varying mantle conductance, *Phys. Earth Planet. Int.*, 117, 329-344, 2000.
- Hulot, G., Eymin, C., Langlais, B., Mandea, M., Olsen, N., Small-scale structure of the geodynamo inferred from Oersted and Magsat satellite data, *Nature*, 416, 620-623, 2002.
- Jacobs, J.A., *Reversals of the Earth's magnetic field*, Adam Hilger Ltd, Bristol, 1984.
- Jackson, A., Jonkers, A.R.T., Walker, M.R., Four centuries of geomagnetic secular variation from the historical records, *Phil. Trans. R. Soc. London A*, 358, 957-990, 2000.
- Johnson, C.L., Constable, C.G., Persistently anomalous Pacific geomagnetic fields, *Geophys. Res. Lett.*, 25, 1,011-1,014, 1998.
- Knittle, E., The solid-liquid partitioning of major and radiogenic elements at lower mantle pressures: *The Core-Mantle Boundary Region*, M. Gurnis, M.E. Wysession, E. Knittle, B.A. Buffett editors, 119-130, 1998.

- Knittle, E. Jeanloz, R., Melting curve of  $(Mg, Fe)SiO_3$  perovskite to 96 GPa: Evidence for a structural transition in lower mantle melts, *Geophys. Res. Lett.*, 16, 609-612, 1989.
- Knittle, E. Jeanloz, R., The Earth's core-mantle boundary: results of experiments at high pressures and temperatures, *Science*, 251, 1438-1443, 1991.
- Koyama, T., Shimizu, H., Hisashi U., Possible effects of the lateral heterogeneity in the  $D''$  layer on electromagnetic variations of core origin, *Phys. Earth Planet. Int.*, 129, 99-116, 2002.
- Laj, C., Mazaud, A., Weeks, R., Fuller, M., Herrero-Bervera, E., Geomagnetic reversal paths, *Nature*, 351, 447, 1991.
- Laj, C., Mazaud, A., Weeks, R., Fuller, M., Herrero-Bervera, E., Geomagnetic reversal paths, *Nature*, 359, 111-112, 1992.
- Langel, R.A., The Main Field, *Geomagnetism*, Vol. 1, J.A. Jacobs editor, Academic Press, London, UK, 249-492, 1987.
- Langel, R.A., International Geomagnetic Reference Field, 1991 revision: IAGA Division V, Working Group 8: Analysis of the main field and secular variation, *Phys. Earth Planet. Int.*, 70, 1-6, 1992.
- Langereis, C.G., van Hoof, A.A.M., Rochette, P., Longitudinal confinement of geomagnetic reversal paths as a possible sedimentary artefact, *Nature*, 358, 226-230, 1992.
- Lay T., Williams, Q., Garnero, E.J., The core-mantle boundary layer and deep Earth dynamics, *Nature*, 392, 461-468, 1998.
- Liddicoat, J.C., Gauss - Matuyama polarity transition, *Phil. Trans. R. Soc. London*, A, 121-128, 1982.

- Love, J.J., Paleomagnetic volcanic data and geomagnetic regularity of reversals and excursions, *J. Geophys. Res.*, 103, 12,435-12,452, 1998.
- Love, J.J., Statistical assessment of preferred transitional VGP longitudes based on paleomagnetic lava data, *Geophys. J. Int.*, 140, 211-221, 2000.
- Merill, D.T., McElhinny, M.W., *The Earth's Magnetic Field*, 1st edition, Academic Press Inc., 1983.
- Olson, P., The disappearing dipole, *Nature*, 416, 591-594, 2002.
- Opdyke, N.D., Glass, B., Hays, J.D., Foster J., Paleomagnetic study of Antarctic deep-sea cores, *Science*, 154, 349, 1966.
- Opdyke, N.D., Kent, D.V., Lowrie, W., Details of magnetic polarity transitions recorded in a high deposition rate deep-sea core, *Earth Planet. Sci. Lett.*, 20, 315, 1973.
- Poirer, J.-P., Le Mouél, J.-L., Does infiltration of core material into the lower mantle affect the observed magnetic field?, *Phys. Earth Planet. Int.*, 73, 29-37, 1992.
- Poirer, J.-P., Malavergne V., Le Mouél, J.-L., Is there a thin electrically conducting layer at the base of the mantle?, *The Core-Mantle Boundary Region*, M. Gurnis, M.E. Wyssession, E. Knittle, B.A. Buffett editors, 119-130, 1998.
- Prévot, M., Camps, P., Absence of preferred longitude sectors for poles from volcanic records of geomagnetic reversals, *Nature*, 366, 53-57, 1993.
- Quidelleur, X., Courtillot, V., On low degrees of paleo-secular variation, *Phys. Earth Planet. Int.*, 95, 55-77, 1996.
- Runcorn, S.K., Polar paths in geomagnetic reversals, *Nature*, 356, 654-656, 1992.
- Shankland, T.J., Peyronneau, J., Poirer, J.P., Electrical conductivity of the Earth's lower mantle, *Nature*, 366, 453-455, 1993.



- Smylie, D.E., Magnetic diffusion in a spherically symmetric conducting mantle, *Geophys. J. R. Astr. Soc.*, 9, 169-184, 1965.
- Stevenson, D.J., Material transport across the core-mantle boundary, *EGU-AGU-EGS Geophys. Res. Abstr.*, 5, 03290, 2003.
- Steinbach, V., Yuen, D.A., Viscous heating: a potential mechanism for the formation of the ultralow velocity zone, *Earth Planet. Scie. Lett.*, 172, 213-220, 1999.
- Tauxe, L., SIO 247, *Rock and paleomagnetism Course Notes*, Scripps Institution of Oceanography, 2002.
- Tric, E., Laj, C., Jehanno C., Valet, J.-P., Kissel, C., Mazaud, A., Iaccarino, S., High-resolution record of the Upper Olduvai transition from Po Valley (Italy) sediments - Support for a dipolar transition geometry, *Phys. Earth Planet. Int.*, 65, 319-336, 1991.
- Valet, J.-P., Turcholka, P., Courtillot, V., Meynardier, L., Paleomagnetic constraints on the geometry of the geomagnetic field during reversals, *Nature*, 356, 400-407, 1992.
- Williams, Q., Garnero, E.J., Seismic evidence for partial melt at the base of Earth's mantle, *Science*, 273, 1,528-1,530, 1996.
- Williams, Q., Revenaugh, J.S., Garnero, E.J., A correlation between ultra-low basal velocities in the mantle and hot spots, *Science*, 281, 546-549, 1998.